THz Beam Shaping through Laser Filamentation Engineering

Dimitra K. Pappa

Department of Physics, University of Crete

Supervised by: Stelios Tzortzakis

September 2024

Acknowledgements

Abstract

Terahertz (THz) beam profile shaping has an essential role in an extensive spectrum of scientific, industrial, and technological applications, among them high-resolution imaging, spectroscopic analysis, advanced communication systems, and material processing. Classical methods for modifying the THz beam profile, such as diffractive optical elements, metasurfaces, and wavefront phase manipulation, have proven beneficial; nevertheless, they tend to be associated with supplementary system complexity or losses of power. In this present study, we suggest a novel approach for controlling the shape and the energy distribution of a broadband THz beam by manipulating the THz source directly. In our experimental setup, ultrashort laser pulses (800 nm, 35 fs, 2 mJ/pulse, 1 kHz) and their second harmonic deliver a typical two – color laser filamentation process in air, which produces THz radiation. To shape the THz beam, we use a Spatial Light Modulator (SLM) that operates at the initial laser frequency and produces diverse laser energy distributions. By creating off-axis spherical phases, the SLM allows the development of different laser filaments across multiple spatial arrangements. This technique enables us to alter the classical doughnut – shaped THz beam profile that results from a single filament, leading to additional complicated beam profiles when two or more filaments are positioned in varied geometries. The method we developed provides the entire electronic control of the beam profile by employing phase masks on the SLM, resulting in dynamic and adaptable THz beam shaping. When the filaments are significantly separated, the resulting beam profiles can be attributed to either linear interference effects or nonlinear energy redistribution through Kerr cross – talk when the filaments are sufficiently close to one another. This all – optical approach, recognized for its straightforwardness and simplicity of execution, presents promising applications in THz imaging and beam engineering, notably in the field of telecommunications. Our outcomes illustrate that by directly controlling the laser – induced filamentation process, we can obtain flexible and efficient manipulation of THz beam shaping, setting up potential opportunities for the development of advanced THz technologies.

Table of Contents

Chapter 1

Introduction

1.1 Basics of THz Radiation

1.1.1 THz Radiation: An Overview and Key Properties

The electromagnetic spectrum encompasses a range of electromagnetic waves stretching from gamma rays to radio waves, each characterized by different frequencies. In recent years, the Terahertz (THz) frequency range (1 THz = 10^{12} Hz) has been recognized as a particularly intriguing area of the electromagnetic spectrum for learning about numerous scientific phenomena. THz radiation spans electromagnetic waves with frequencies ranging from 0.1 THz to 30 THz, which corresponds to wavelengths extending from approximately 3 mm to 10 μm. This range is commonly referred to as the "THz gap" because it is located among the well – explored microwave and infrared (IR) parts of the electromagnetic spectrum, as shown in *Figure 1.1*. Over the years, the THz gap has been nearly impossible to exploit since there are challenges with generating and detecting THz radiation successfully. Nevertheless, as laser and photonics technology have advanced, the THz domain has established itself as a significant field for both research and application in everyday life [1].

THz radiation contains photon energies that vary between 0.4 and 120 meV and are considerably weaker than the ones of visible light, ultraviolet (UV) radiation, and X – Rays. THz radiation is categorized as non – ionizing since its photon energies are insufficient to ionize atoms or molecules, making it fundamentally harmless compared to higher – energy radiation types [2][3].
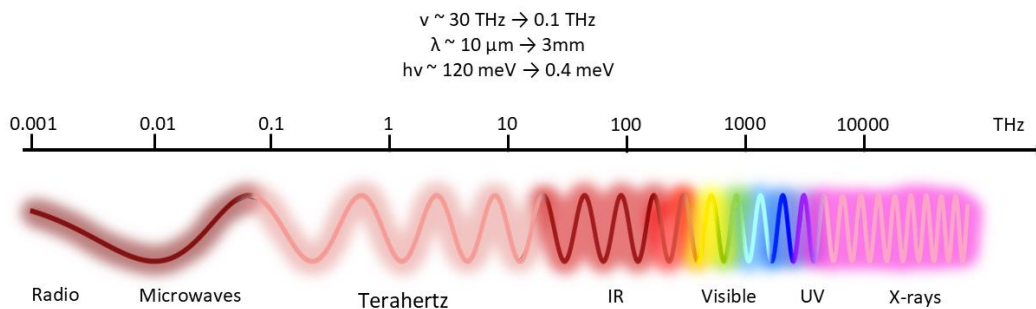
Figure 1.1: The electromagnetic spectrum highlighting the THz range, showing its placement between microwaves and infrared light, with corresponding frequency, wavelength, and photon energy ranges.

One of the most important characteristics of THz radiation is its non – ionizing nature, which makes it appropriate for an extensive variety of applications requiring safety. In juxtaposition with ionizing radiation such as UV or X – Rays that might remove electrons from atoms and induce molecular damage, THz photons have energy that is substantially lower than the ionization threshold for the majority of materials, usually about a few electron volts (eV) [4]. THz radiation's low energy precludes it from inflicting the cellular and genetic damage associated with ionizing radiation, therefore rendering it a promising candidate for biomedical imaging, security scanning, and various other non – destructive testing applications [5].

In one instance, in biomedical imaging, THz radiation is currently being studied for its ability to detect and discriminate between various tissue categories. The interaction of THz waves with biological tissues, which is determined by the tissue's water content and other features, offers a non – invasive imaging approach that minimizes potential risks that arise from ionizing radiation [6].

Strong interactions between THz radiation and water molecules result in high coefficients of absorption in aqueous environments, which is an important feature of THz radiation. Water's absorption spectrum in the THz range can be identified by resonances that correspond to rotational and vibrational transitions, which lead THz waves to be rapidly absorbed in moist or hydrated materials. This means that absorption can limit the penetration depth of THz radiation, especially in biological tissues containing a high percentage of water [7] [8].

Notwithstanding this limitation, the remarkable sensitivity of THz radiation to water concentration has been used in a number of applications. For instance, in pharmaceuticals, THz spectroscopy can be utilized to monitor tablet moisture content during production, providing critical information about product quality and standardization. In an analogous manner in agricultural science, THz radiation is employed for estimating crop moisture level, which is important for calculating harvest times and storage conditions [2]. Furthermore, medical diagnostics exploit THz radiation's water absorption capabilities to recognize and visualize tissue abnormalities. Because diseased tissues typically contain different water contents than
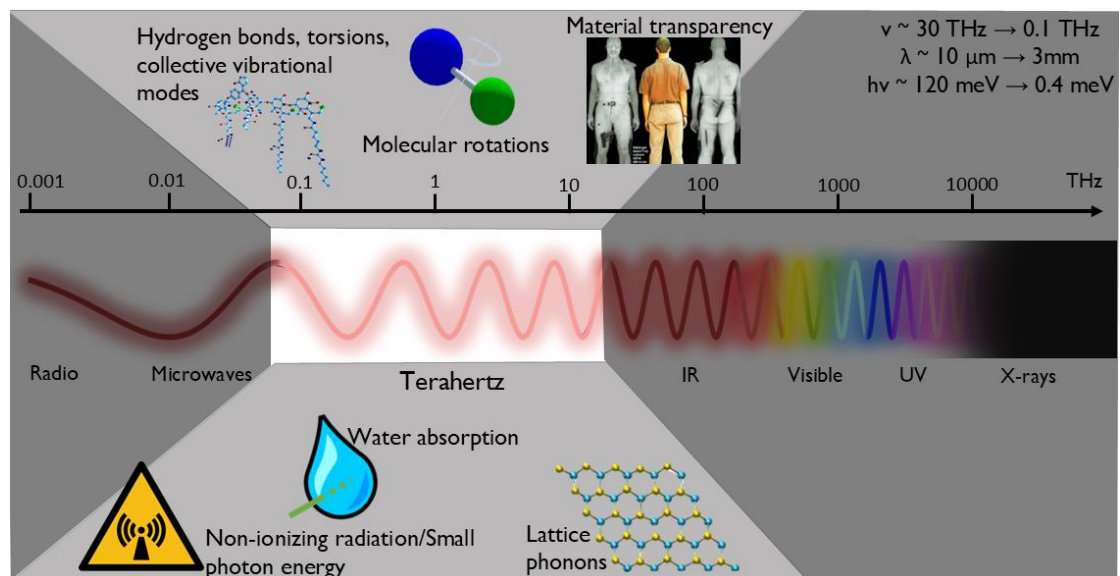

Figure 1.2: An overview of THz radiation properties, including molecular rotations, hydrogen bonds, torsions, water absorption, and material transparency. The diagram emphasizes the non – ionizing nature of THz radiation and its interaction with water and other materials.

healthy tissues, THz imaging can provide contrast based on these variations, suggesting a non – invasive method for diagnosing conditions such as cancer or skin disorders [9].

THz radiation is exceptionally advantageous in studying low – energy molecular dynamics, such as molecular rotations, hydrogen bonding, torsional oscillations, and collective vibrational modes. These interactions develop at energy levels equivalent to the photon energies of THz radiation, making THz spectroscopy a powerful tool for exploring these kinds of phenomena [10]. As an example, THz time – domain spectroscopy (THz – TDS) permits direct observation of molecular movements and interactions in a broad spectrum of materials, from simple gases to complicated biological macromolecules. This technique has been applied to analyze the hydration shells of proteins, where water molecules interact via hydrogen bonds, as well as the dynamical behavior of DNA and other biomolecules [11].

In addition, THz radiation's ability to look into collective vibrational modes in materials makes it extremely beneficial for researching phase transitions and other changes in structure. In crystalline solids, for example, THz radiation can be employed to observe lattice phonons, which are quantized atom vibrations within a crystal lattice. These phonons possess a significant role in determining materials' thermal and electrical properties, which makes THz spectroscopy an invaluable tool for material science research [12].

Transparency to certain non-polar materials, such as polymers, fabrics, ceramics, and some dry biological tissues, is another important characteristic of THz radiation. These materials possess poor THz absorption, letting THz waves pass through deeply, making THz radiation an ideal choice for non – destructive testing and imaging [13]. THz imaging systems, for example, serve in the security industry to detect concealed weapons and contraband hidden beneath clothing. THz radiation, which may penetrate fabrics but is reflected or absorbed by metals and other dense materials, offers a non – invasive method for screening individuals. Likewise, in industrial applications, THz imaging can be utilized to analyze the internal structure of composite materials, recognize imperfections or inclusions, and verify the quality of products, among them pharmaceuticals and food items [14].

The material transparency in the THz range has additionally been used in cultural heritage preservation, where THz imaging is utilized to examine the internal layers of artworks and historically significant objects without damaging them. This capability has revealed novel perspectives into the processes and materials used by artists, as well as assisting conservators in determining the condition of aging artworks [15].

1.1.2 THz Radiation: A Spectrum of Applications

THz radiation, with frequencies ranging from 0.1 THz to 30 THz, has emerged as a potent tool in a variety of scientific and industrial domains thanks to the distinctive characteristics detailed above. These include its non – ionizing properties, ability to penetrate non – conductive materials, and sensitivity to water content. The following section delves into five major applications of THz radiation: biomedicine, security, automotive, pharmacy, and telecommunications. Each division highlights multiple benefits of THz technology and how it is applied in various fields.

THz radiation has significant biomedical applications, especially in medical imaging and diagnostics. Its ability to differentiate among tissue types based on water content makes it an important tool for noninvasive imaging. THz imaging, for instance, has been employed effectively to detect and differentiate between malignant and benign tissues, particularly in the

diagnosis of skin and breast cancer [1]. The contrast between malignant and healthy tissues stems from differences in dielectric characteristics, which are affected by water concentration and molecular composition.

In brain imaging, THz technology has been used to visualize the development of neurological diseases like Alzheimer's. Li et al. (2020) demonstrated the use of THz imaging to detect cognitive impairments that result from a number of factors, highlighting its sensitivity to alterations in brain tissue composition [16]. This ability to spot small fluctuations in the level of water and other molecular structures offers important insights into disease progression, perhaps resulting in earlier diagnosis and improved treatment outcomes. Furthermore, THz spectroscopy is employed for measuring tissue hydration, which is critical in wound recovery and burn treatment. THz radiation's non – destructive nature enables continual monitoring without causing damage to delicate tissues [3].

Moreover, THz radiation is constantly being applied in security applications, primarily for screening and identifying concealed dangers. Its capability to pass through nonmetallic materials, including clothing, paper, and plastics, makes it a promising candidate for the detection of hidden weapons, explosives, and contraband. THz imaging systems may recognize objects based on their distinctive spectral signatures, thereby permitting security personnel to easily differentiate between innocuous and possible threats [17].

Comprehensive studies have demonstrated the efficacy of THz spectroscopy in detecting explosives and drugs. Research has found that THz time – domain spectroscopy (THz – TDS) could possibly identify and differentiate between diverse substances, as well as those contained within packaging materials [18]. This ability is particularly beneficial in airport security, where non – invasive and quick screening methods must take place. On top of that, the arrival of portable THz scanners has increased the use of THz technology in field operations by law enforcement agencies. These types of scanners can detect hidden objects on individuals or in vehicles, strengthening public safety without the need for intrusive searches [11].

The automotive industry is yet another area where THz radiation is making an enormous contribution. One of its principal services is non – destructive testing (NDT) of materials, specifically composite materials used in vehicle construction. THz radiation can identify interior complications such as delamination, voids, and cracks that may jeopardize the structural quality of vehicle components [19]. A study found that THz imaging may assess the thickness and consistency of paint coats, detect imperfections in structure, and guarantee the overall
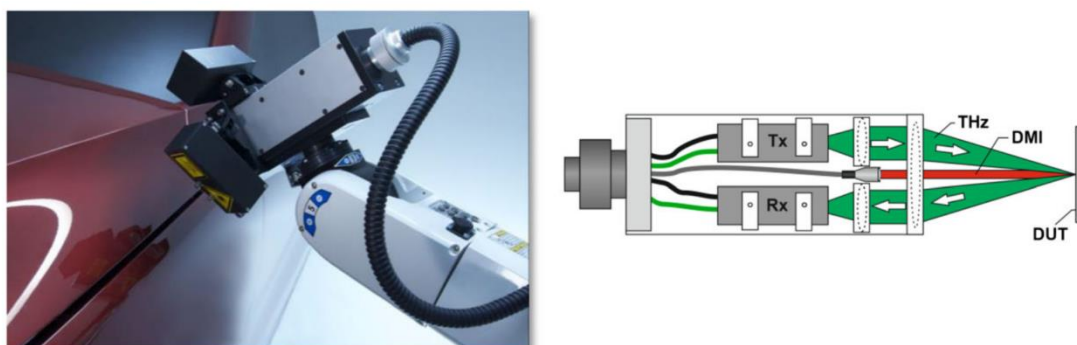

Figure 1.3: (Left) a THz sensor mounted on a robot during the measurement of individual layer thicknesses of a multilayer painting on a car body. (Right) Schematic representation of a pitch – catch terahertz transceiver comprising an integrated displacement-measuring interferometer sensor for the compensation of vibration.

quality of automobile parts. The aforementioned application not only improves safety but also encourages manufacturers to maintain high production quality standards [20].

In furtherance of quality control, THz sensors are being implemented into advanced driver assistance systems (ADAS) to increase vehicle safety. These kinds of sensors are capable of seeing objects in low-visibility environments, such as fog or heavy rain, where common optical systems may actually fail. This ability optimizes collision detection and avoidance systems, resulting in safer driving experiences [21].

THz spectroscopy has proven to be a successful tool in the pharmaceutical industry, notably for the analysis of solid dosage forms. THz imaging provides non – destructive inspection of tablets and capsules, guaranteeing that active pharmaceutical ingredients (APIs) are evenly dispersed and that there are no imperfections or inconsistencies [14]. One of the essential applications of THz radiation in the pharmaceutical sector is to measure tablet coating thickness. The coating thickness is critical for managing the drug's release rate, and THz imaging offers a precise, real – time method for determining this during manufacture. This application minimizes waste while ensuring that every single batch fulfills the required quality criteria [22].

Likewise, Davies et al. (2008) discussed the use of THz spectroscopy to detect counterfeit pharmaceuticals. The study demonstrated that THz spectroscopy could differentiate between authentic and counterfeit drugs based on their characteristic spectral signatures, thus rendering it an effective tool for guaranteeing drug safety and integrity [18].

As the demand for enhanced data transfer speeds increases, the telecommunications field is exploring the use of THz frequencies in next – generation wireless communication systems. THz waves have the potential for ultra – high – speed data transport, allowing the development of 6G and beyond networks [23]. THz radiation's high frequency allows data transmission rates that far exceed those possible with current microwave and millimeter – wave technologies. This technological breakthrough has the potential to revolutionize wireless communications by allowing for faster internet speeds, more dependable connections, and the ability to serve a wider range of connected devices in densely populated areas [24].

1.2 THz Generation Mechanisms: An Overview

Among the most frequently applied techniques for producing THz radiation are optical rectification and photoconductive antennas. These methods generate THz radiation by interacting ultrafast laser pulses with materials, but their fundamental principles differ.

Photoconductive antennas (PCAs) are one of the most used methods for producing and detecting THz radiation. The operation of a PCA is based on the stimulation of charge carriers in semiconductor material using an ultrafast laser pulse. A femtosecond laser pulse lights a semiconductor substrate (often low – temperature – grown gallium arsenide, LT – GaAs), which is biased by an external electric field. Photon absorption from the laser pulse causes electrons to move from the valence band to the conduction band, forming electron-hole pairs within the semiconductor. The electric field across the semiconductor substrate accelerates charge carriers, resulting in a transient current. This ultrafast current, which lasts a few picoseconds, emits electromagnetic waves of THz frequency ranges [25]. The temporal properties of the laser pulse are important in determining the bandwidth of the emitted THz radiation. Femtosecond pulses of shorter duration produce broader THz spectra, but longer pulses limit THz bandwidth. In addition, the lifetime of charge carriers in the semiconductor is necessary for the efficiency of

the THz generating process. Materials with short carrier lifetimes, such as LT – GaAs, are commonly used because they allow a faster current decay and hence a more efficient emission of THz radiation. PCAs have been widely used in THz time-domain spectroscopy (THz – TDS) systems to both generate and detect THz radiation [6].

On the contrary, optical rectification, which occurs when powerful femtosecond laser pulses interact with nonlinear optical crystals, is another important process for THz production. Optical rectification is a second – order nonlinear optical process in which the electric field of an incident laser pulse induces a polarization in the crystal. This temporally change in polarization, which oscillates at the frequency of the laser pulse, causes a nonlinear response, resulting in the THz radiation production [26]. Unlike photoconductive antennas, which generate and accelerate charge carriers, optical rectification uses the crystal's intrinsic nonlinear characteristics to produce radiation. Common optical rectification materials include zinc telluride (ZnTe), gallium phosphide (GaP), and lithium niobate (LiNbO$_3$) [27]. Several parameters influence optical rectification efficiency, including phase matching between laser pulse and generated THz wave. Phase matching ensures that the resultant THz radiation is coherent as it passes through the crystal, allowing for effective energy conversion from the optical pulse to the THz field. The interaction length, or distance over which phase matching is maintained, is crucial in establishing the output power and bandwidth of THz radiation [28]. Optical rectification is an efficient method for producing high – energy THz pulses, especially in setups where phase matching may be tuned. It is commonly used in research and industrial applications that demand intense THz radiation over a broad spectral range.

While photoconductive antennas and optical rectification are well-known ways for producing THz, alternative methods capable of producing larger THz field strengths and broader spectral coverage have been thoroughly studied for many years. One such technique is to generate THz radiation through two – color laser filamentation in the air, which takes advantage of the interaction between ultrafast laser pulses and gases. The chapter that follows will provide an in – depth review of THz generation using two – color laser filamentation, diving into the underlying physics such as nonlinear optical effects, plasma dynamics, and phase matching conditions. This unique method represents a significant advancement in THz technology, opening up novel possibilities for THz beam shape and control.

References

1. Siegel, P. H. (2004). Terahertz Technology in Biology and Medicine. *IEEE Transactions on Microwave Theory and Techniques*, *52*(10), 2438–2447. https://doi.org/10.1109/TMTT.2004.835916

2. Tonouchi, M. (2007). Cutting-edge terahertz technology. *Nature Photonics*, *1*(2), 97-105 https://doi.org/10.1038/nphoton.2007.3

3. Mittleman, D. (Ed.). (2003). *Sensing with Terahertz Radiation* (Vol. 85). Springer. https://doi.org/10.1007/978-3-540-45601-8

4. Ferguson, B., & Zhang, X.-C. (2002). Materials for terahertz science and technology. *Nature Materials*, *1*(1), 26–33. https://doi.org/10.1038/nmat708

5. Pickwell, E., & Wallace, V. P. (2006). Biomedical applications of terahertz technology. *Journal of Physics D: Applied Physics*, *39*(17), R301. https://doi.org/10.1088/0022-3727/39/17/R01

6. Jepsen, P. u., Cooke, D. g., & Koch, M. (2011). Terahertz spectroscopy and imaging – Modern techniques and applications. *Laser & Photonics Reviews*, *5*(1), 124–166. https://doi.org/10.1002/lpor.201000011

7. Kawase, K., Ogawa, Y., Watanabe, Y., & Inoue, H. (2003). Non-destructive terahertz imaging of illicit drugs using spectral fingerprints. *Optics Express*, *11*(20), 2549–2554. https://doi.org/10.1364/OE.11.002549

8. Fischer, B. M., Walther, M., & Jepsen, P. U. (2002). Far-infrared vibrational modes of DNA components studied by terahertz time-domain spectroscopy. *Physics in Medicine & Biology*, *47*(21), 3807. https://doi.org/10.1088/0031-9155/47/21/319

9. Giovannacci, D., Dominique, M.-L., Walker, G., Menu, M., & Detalle, V. (2013). *Terahertz applications in cultural heritage: Case studies*. *9065*, 906510. https://doi.org/10.1117/12.2049818

10. Fitzgerald, A. J., Berry, E., Miles, R. E., Zinovev, N. N., Smith, M. A., & Chamberlain, J. M. (2002). Evaluation of image quality in terahertz pulsed imaging using test objects. *Physics in Medicine and Biology*, *47*(21), 3865–3873. https://doi.org/10.1088/0031-9155/47/21/326

11. Cooper, K., Dengler, R., Llombart, N., Thomas, B., Chattopadhyay, G., & Siegel, P. (2011). THz Imaging Radar for Standoff Personnel Screening. *Terahertz Science and*

Technology, IEEE Transactions On, *1*, 169–182. https://doi.org/10.1109/TTHZ.2011.2159556

12. Schmuttenmaer, C. A. (2004). Exploring Dynamics in the Far-Infrared with Terahertz Spectroscopy. *Chemical Reviews*, *104*(4), 1759–1780. https://doi.org/10.1021/cr020685g

13. Koulouklidis, A. D. (2016). *Intense Broadband THz Fields from Laser-Plasma Interactions* [PhD Thesis, University of Crete]. https://doi.org/10.12681/eadd/39960

14. Shen, Y. C., Lo, T., Taday, P. F., Cole, B. E., Tribe, W. R., & Kemp, M. C. (2005). Detection and identification of explosives using terahertz pulsed spectroscopic imaging. *Applied Physics Letters*, *86*(24), 241116. https://doi.org/10.1063/1.1946192

15. Woodward, R. M., Wallace, V. P., Arnone, D. D., Linfield, E. H., & Pepper, M. (2003). Terahertz Pulsed Imaging of Skin Cancer in the Time and Frequency Domain. *Journal of Biological Physics*, *29*(2), 257–259. https://doi.org/10.1023/A:1024409329416

16. Li, J., Liu, M., Gao, J., Jiang, Y., Wu, L., Cheong, Y.-K., Ren, G., & Yang, Z. (2020). AVNP2 protects against cognitive impairments induced by C6 glioma by suppressing tumour associated inflammation in rats. *Brain, Behavior, and Immunity*, *87*. https://doi.org/10.1016/j.bbi.2020.02.009

17. Federici, J. F., Schulkin, B., Huang, F., Gary, D., Barat, R., Oliveira, F., & Zimdars, D. (2005). THz imaging and sensing for security applications—Explosives, weapons and drugs. *Semiconductor Science and Technology*, *20*(7), S266. https://doi.org/10.1088/0268-1242/20/7/018

18. Davies, A., Burnett, A., Fan, W., Linfield, E., & Cunningham, J. (2008). Terahertz spectroscopy of explosives and drugs. *Materials Today - MATER TODAY*, *11*, 18–26. https://doi.org/10.1016/S1369-7021(08)70016-6

19. Stoik, C. D., Bohn, M. J., & Blackshire, J. L. (2008). Nondestructive evaluation of aircraft composites using transmissive terahertz time domain spectroscopy. *Optics express*, *16*(21), 17039–17051. https://doi.org/10.1364/oe.16.017039

20. Ellrich, F., Bauer, M., Schreiner, N., Keil, A., Pfeiffer, T., Klier, J., Duran, S., Jonuscheit, J., Friederich, F., & Molter, D. (2020). Terahertz Quality Inspection for Automotive and Aviation Industries. *Journal of Infrared, Millimeter, and Terahertz Waves*, *41*. https://doi.org/10.1007/s10762-019-00639-4

21. Kleine-Ostmann, T., & Nagatsuma, T. (2011). A Review on Terahertz Communications Research. *Journal of Infrared, Millimeter, and Terahertz Waves*, *32*(2), 143–171. https://doi.org/10.1007/s10762-010-9758-1

22. Zeitler, J. A., Shen, Y., Baker, C., Taday, P. F., Pepper, M., & Rades, T. (2007). Analysis of coating structures and interfaces in solid oral dosage forms by three-dimensional

terahertz pulsed imaging. *Journal of Pharmaceutical Sciences*, *96*(2), 330–340. https://doi.org/10.1002/jps.20789

23. Kürner, T., & Priebe, S. (2014). Towards THz Communications—Status in Research, Standardization and Regulation. *Journal of Infrared, Millimeter, and Terahertz Waves*, *35*(1), 53–62. https://doi.org/10.1007/s10762-013-0014-3

24. Nagatsuma, T., Ducournau, G., & Renaud, C. C. (2016). Advances in terahertz communications accelerated by photonics. *Nature Photonics*, *10*(6), 371–379. https://doi.org/10.1038/nphoton.2016.65

25. *Principles of Terahertz Science and Technology*. (2009). Springer US. https://doi.org/10.1007/978-0-387-09540-0

26. Shen, Y. R. (1984). *The Principles of Nonlinear Optics*. Wiley-Interscience.

27. Boyd, R. W. (2008). *Nonlinear Optics (Third Edition)* (pp. 1–67). Academic Press. https://doi.org/10.1016/B978-0-12-369470-6.00001-0

28. Hebling, J., Almási, G., Kozma, I. Z., & Kuhl, J. (2002). Velocity matching by pulse front tilting for large-area THz-pulse generation. *Optics Express*, *10*(21), 1161–1166. https://doi.org/10.1364/OE.10.001161

Chapter 2

THz Emission through Laser Filamentation

2.1 Nonlinear Propagation

A brief introduction of the fundamental nonlinear – optical phenomena that lead to femtosecond laser filamentation and THz emission is provided in this chapter. At low light intensities, which are typical of non-laser sources, material characteristics remain unaffected by illumination intensity. In this regime, the superposition principle is applicable, allowing light waves to pass through materials or be reflected from limits and interfaces without any interaction. On the other hand, high – power laser pulses possess the ability to temporally modify a medium's optical properties and induce non – linear polarization in materials. The waves of light are able to interact with one another, transferring velocity and energy, while the superposition principle no longer holds. This interaction of light waves can produce optical fields with new frequencies, such as optical harmonics of incident radiation or sum – or difference – frequency signals [1]. The nonlinear propagation of ultrashort laser pulses controls the production of THz radiation through laser filamentation in air. Understanding how the laser pulse evolves as it propagates through the medium and forms stable filaments requires knowledge of the key nonlinear effects that are involved, specifically the Optical Kerr Effect, Optical Field Ionization (OFI), and laser filamentation. Since the filaments concentrate the laser energy and establish the conditions required for nonlinear interactions, they are necessary to the effective production of THz radiation.

2.1.1 Optical Kerr Effect

The phenomenon known as the Kerr Effect unfolds when a material's refractive index changes in response to an applied electric field [2]. An analogous effect appears within the field of nonlinear optics, where laser light causes the electric field to be dynamic and oscillate rapidly. The fundamental mechanism underpinning femtosecond laser filamentation has become known as the optical Kerr effect. This phenomenon not only leads to filamentation but also supports a broad variety of nonlinear optical phenomena, namely self – phase modulation, four – wave mixing, and third – harmonic production. When a medium, such as air or any transparent material, is exposed to a vigorous laser field, its refractive index is affected not only by the frequency of the laser field but additionally by its intensity with respect to the spatial and

temporal distribution. Mathematically, the intensity – dependent refractive index n(I) can be described by the equation:

$$n(I) = n_0 + n_2 I(r,t) \tag{2.1}$$

where n_0 represents the linear refractive index, n_2 is the nonlinear refractive index, and $I(r,t)$ is the intensity of the laser field at a given position and time [2]. The nonlinear refractive index coefficient n_2 is a significant parameter in determining the extent of the Kerr effect, and it varies significantly among media. For gases, n_2 is commonly around 10^{-19} cm^2/W, but in amorphous solids and liquids, it is on the order of 10^{-16} cm^2/W [3]. This considerable disparity in n_2 values explains why nonlinear optical effects, such as self – focusing, are more noticeable in solids and liquids rather than gases. This equation states that the refractive index of a laser beam as it propagates through a nonlinear material is inextricably related to the intensity profile of the beam itself. As an aftermath, a beam with a Gaussian intensity profile induces a corresponding Gaussian modulation in the refractive index, consequently forming a self – induced lens. This lens – like modulation allows the beam to focus as it propagates, a phenomenon called self – focusing.

P. L. Kelley conducted the first systematic study of self – focusing, in which a beam can focus itself regardless of the need for external optical components [4]. Following then, it has been intensively studied and nonetheless remains an important topic in nonlinear optics [5]. Self – focusing is especially relevant in media with a positive nonlinear refractive index ($n_2 > 0$), where the effect can be observed even at low intensities. However, for self – focusing to outperform natural beam diffraction, the beam's power must reach a crucial threshold known as the critical power for self – focusing (P_{cr}). For Gaussian beams, the critical power P_{cr} can be expressed by the equation:

$$P_{cr} = \frac{3.77\lambda_0^2}{8\pi n_0 n_2} \tag{2.2}$$

where λ_0, is the wavelength of the laser light [6]. The above equation demonstrates that the critical power is not reliant on the intensity of the beam but rather on the wavelength and nonlinear characteristics of the medium that it passes through. So, for instance, in the air, the critical power for a near – infrared ultrashort laser pulse is around 3.2 GW, whereas in water, with a greater n_2 value, it is around 4 MW [7].
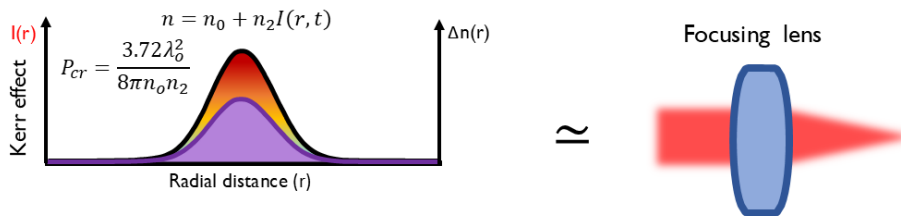
Figure 2.1: The refractive index modulation due to the Kerr Effect is akin to the action of a positive lens, which causes the laser beam to self-focus.

When the laser beam's power exceeds this critical threshold, the Kerr effect causes a focusing behavior, condensing the beam's spatial profile and thus increasing the intensity at its very center. As the intensity of the beam increases at its center, it is capable of ionizing the surrounding atmospheric molecules, thereby creating a plasma channel.

2.1.2 Optical Field Ionization

As a high – intensity laser pulse propagates through a medium, the phenomenon of self – focusing considerably raises the laser intensity I, to the point where the laser pulse's energy is sufficient to ionize the medium's atoms or molecules. Ionization is essential in plasma generation, which has a major impact on the laser beam's propagation characteristics. The primary ionization mechanisms that control this process are multiphoton ionization (MPI) and tunnel ionization.

Figure 2 2: Schematic diagrams that illustrate the processes of a) multiphoton and b) tunnel ionization.

Multiphoton ionization is a highly nonlinear optical process that takes place when an atom or molecule absorbs multiple photons at the same moment. The total energy of these photons surpasses the atom's ionization potential, resulting in the release of an electron. The rate of MPI is co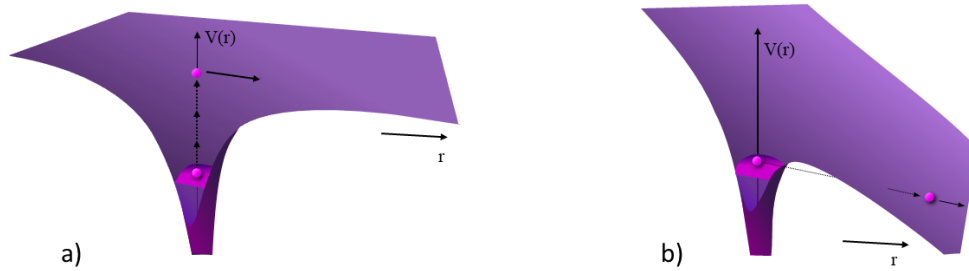nsiderably dependent on the intensity of the laser light, with a power – law relationship written as I^K, where K stands for the number of photons necessary for ionization. Considering only oxygen molecules, K is approximately eight for an 800 nm laser beam propagating in air [8]. In other words, eight photons are required to ionize one oxygen molecule, underscoring the nonlinear nature of MPI, in which the probability of ionization increases dramatically with laser intensity. The process is also wavelength dependent; shorter wavelengths, which correspond to greater photon energies, demand a lower number of photons for ionization, albeit the particular value of K is additionally determined by the material's intrinsic characteristics. In other forms of matter, such as liquids and solids, the value of K is usually lower, indicating variations in nonlinear responses and ionization potentials. For example, an 800 nm laser wavelength ionizes a water molecule with K=5 photons, but K in fused silica glass is roughly 6 [9]. These smaller K values signify that MPI is more efficient in these media at analogous intensities, thus making it easier to ionize molecules in liquids and solids than in gases.

MPI is especially important in the initial stages of laser filamentation, when the laser intensity has not yet reached its peak. At these lower intensities, MPI is the predominant ionization mechanism, triggering the formation of free electrons within the medium. These released electrons, in the meantime, participate in further ionization processes, causing a cascade effect that increases plasma density.

As the laser pulse intensity increases, tunnel ionization becomes the major ionization mechanism. In contrast to MPI, tunnel ionization does not need the simultaneous absorption of multiple photons. Instead, it occurs when the laser's electric field is sufficiently powerful to disrupt the Coulomb potential of the atom, enabling an electron to tunnel through the potential barrier and escape. Tunnel ionization differs from MPI in that it is proportional to the strength of the electric field rather than photon energy. The Keldysh parameter (γ_K) describes the transition from MPI to tunnel ionization as the dominant ionization mechanism. The Keldysh

parameter is dimensionless and indicates which ionization process is more likely to occur under certain laser conditions. The definition is as follows:

$$\gamma_K = \sqrt{\frac{U_i}{2U_p}} = \sqrt{\frac{t_i}{T}} \qquad (2.3)$$

$$U_p = \frac{e^2 E^2}{4m_e \omega^2} \ , \qquad T = \frac{2\pi}{\omega} \qquad (2.4)$$

where U_i is the ionization potential energy of the atom, U_p is the laser ponderomotive potential energy, t_i is the ionization time and T is the laser oscillation period, ω is the angular frequency of the laser, E is the amplitude of the electric field of the laser, m_ε is the electron mass, and e is the elementary charge [9], [10]. The value of γ_K determines the classification of the ionization regime: when γ_K is significantly higher than one ($\gamma_K \gg 1$), multiple photon absorption (MPI) dominates the ionization process since there is insufficient electric field to cause tunneling. When γ_K is less than one ($\gamma_K \ll 1$), tunnel ionization prevails due to the laser's high electric field [11]. Tunnel ionization commonly appears at laser intensities of 10^{14} W/cm^2, when the electric field strength is powerful enough to deliver tunneling. This process is less dependent on laser frequency than MPI; hence, it is the fundamental ionization mechanism in high – intensity regimes, especially during laser filamentation.

The ionization of the medium leads to the formation of plasma, which has a significant impact on the laser beam's propagation properties. Plasma generation causes a local drop in the medium's refractive index, which is necessary for balancing the self-focusing effect that results from Kerr nonlinearity. The reduction in refractive index due to plasma production can be mathematically expressed as follows:

$$n = n_0 - \frac{\rho(r,t)}{2\rho_c} \qquad (2.5)$$

where $\rho(r,t)$ represents the electron density of the generated plasma, and ρ_c denotes the critical plasma density, at which the medium becomes opaque to the laser light. The critical plasma density, ρ_c, is given by:

$$\rho_c = \frac{\varepsilon_0 m_e \omega_0^2}{e^2} \qquad (2.6)$$

where ε_0 is the permittivity of free space, m_e and e is the electron mass and charge, and ω is the angular frequency of the laser [5]. The corresponding reduction in the refractive index functions as a defocusing process, counteracting the Kerr – induced self – focusing. As seen in *Figure 2.3*, plasma formation due to ionization behaves as a defocusing lens, causing the beam to diverge and preventing it from collapsing into a singularity. At this stage, the beam's intensity profile demonstrates a central peak with ionization – induced defocusing around it. This interplay of self – focusing, triggered by the Kerr effect, and plasma – induced defocusing results in a dynamic equilibrium. This state of equilibrium allows the formation of a stable filament that can propagate over long distances while maintaining a relatively homogeneous
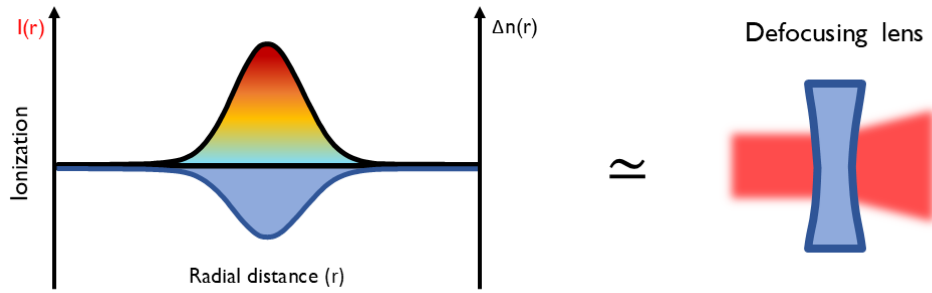
Figure 2.3: The refractive index modulation due to the ionization is akin to the action of a negativw lens, which causes the laser beam to diverge.

intensity profile. The thereby produced filament is a self – guiding structure that is necessary for the beam's stability throughout propagation [7].

To summarize, the ionization processes that occur during self – focusing – multiphoton ionization and tunnel ionization – are critical for understanding laser filament behavior. These processes generate plasma, which alters the medium's refractive index and maintains the filament. Laser filament creation and propagation rely on an accurate equilibrium of self – focusing and defocusing forces.

2.1.3 Filamentation

Filamentation is a phenomenon caused by the precise balance between multiple linear and nonlinear effects on powerful ultrashort laser pulses as they propagate across opaque materials. In the beginning, the laser pulse undergoes linear phenomena that include diffraction and dispersion, which broaden the beam's spatial and temporal profile [12]. As soon as the laser power exceeds a crucial threshold, nonlinear effects, mainly self – focusing, take dominance. The Kerr effect induces self – focusing because the refractive index of the medium increases with the intensity of the light, forcing the beam to converge and its intensity to rise even further, consequently maximizing the self – focusing mechanism [13].

As the beam self – focuses, its intensity increases to levels adequate to ionize the medium using mechanisms that include multiphoton ionization (MPI) and tunneling ionization. MPI is the simultaneous absorption of multiple photons by an atom or molecule, which provides the energy required to eject an electron [16]. On the contrary, tunneling ionization takes place when the laser pulse's strong electric field distorts the atomic potential, letting an electron escape through quantum tunneling [13]. The ionization process creates a plasma, which leads to a local drop in the medium's refractive index. This plasma – induced defocusing counterbalances the Kerr – driven self – focusing and thus stops the beam from collapsing [12].

This interplay of self – focusing and plasma – induced defocusing establishes a dynamic equilibrium that prevents the beam from collapsing into a singularity and promotes the creation of a stable filament. The defocusing plasma spreads the trailing part of the pulse, leading the beam to broaden and its intensity to decrease locally. If the pulse retains sufficient power, it may begin another cycle of self – focusing, consequently perpetuating the filamentation process [16]. This cyclical interaction continues up until the pulse power falls underneath the threshold necessary for self – focusing, at which point linear phenomena including diffraction and dispersion take over, leading to the wavepacket's dispersion [12] [13].
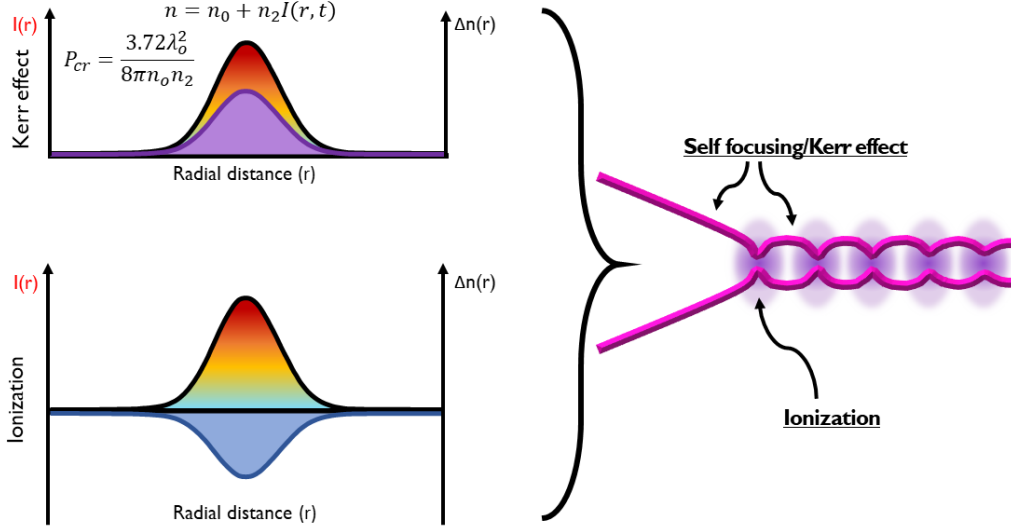
Figure 2.4: A schematic representation of the mechanisms that lead to filamentation. The upper graph illustrates the Kerr effect, while the lower graph shows the ionization leading to the stabilization of the filament.

The dynamic equilibrium between self – focusing and plasma – induced defocusing eventually leads to the creation of a filament, a stable, self – guided structure that maintains high intensity throughout prolonged propagation lengths while exhibiting minimal diffraction [14]. *Figure 2.4* shows the refocusing cycles characteristic of filamentation. Thus, the concept of intensity clamping arises from the direct competition between defocusing and self – focusing mechanisms during filamentation [15]. Intensity clamping is the process of stabilizing the beam's intensity at a maximum level that maintains constant even when the input power increases. The balance between self-focusing and plasma-induced defocusing determines the clamped intensity, reported as I_{cl}, which can be expressed as:

$$I_{cl} \cong \left(\frac{2n_2\rho_c}{\sigma_K t_p \rho_{at}} \right)^{K-1} \qquad (2.7)$$

where n_2 is the nonlinear refractive index, ρ_c is the critical plasma density, σ_K is the ionization cross – section for K photons, t_p is the pulse duration, and ρ_{at} is the density of neutral atoms [16].

Nevertheless, describing filamentation only using the aforementioned dynamic equilibrium is unnecessarily simplistic. Filamentation additionally incorporates nonlinear processes such as self – phase modulation (SPM), which comes from the nonlinear phase shift caused by the intensity – dependent refractive index, resulting in the spectrum broadening of the pulse [16]. Self – steepening is another nonlinear effect that takes place when the leading and trailing edges of a pulse propagate at different speeds due to intensity gradients, resulting in pulse asymmetry [12]. On top of that, losses from multiphoton absorption and plasma absorption have a major impact on the energy distribution inside the pulse, affecting the filamentation process [13]. Whereas these effects are secondary compared to self – focusing and defocusing, they play substantial roles when assessing the filament's properties and stability [8].

2.2 THz Radiation Generation through Two – Color Laser Filamentation in Air: Four Wave Mixing and Photocurrent Models

THz radiation generation via two-color laser filamentation in air has become a well-established approach due to its ability to produce powerful, broadband THz pulses. The Four – Wave Mixing (FWM) and Photocurrent models are two fundamental theoretical frameworks that explain THz methods of production. These models explain how the interplay of laser pulses at the fundamental (ω) and second harmonic (2ω) frequencies results in THz emission. Both of these approaches emphasize the importance of phase control between laser fields in optimizing THz output.

The Four – Wave Mixing (FWM) model is a fundamental concept in nonlinear optics that explains the way the different frequency components in a medium interact in order to create new frequencies. When fundamental (800 nm) and second harmonic (400 nm) laser pulses propagate through air, they generate a nonlinear polarization that oscillates at THz frequencies. The nonlinear polarization P_{NL} that emits THz in the FWM process can be expressed as:

$$\widetilde{P}_{NL} = \varepsilon_0 \chi^{(3)} \widetilde{E}^{(3)}(t) \tag{2.8}$$

where ε_0 is the permittivity of free space, $\chi^{(3)}$ is the third – order nonlinear susceptibility of the medium, and $\widetilde{E}$ the applied electric field [12]. This polarization leads to the emission of THz radiation. Such third – order interactions are common in the optical region, particularly in gases, such as air, where nonlinearity is weaker compared to more condensed media like liquids or solids [16]. The nonlinear susceptibility $\chi^{(3)}$, which controls the strength of field interaction, is a crucial factor in determining the efficiency of the FWM process. Air has a lower value of $\chi^{(3)}$ compared to other nonlinear media, such as crystals or fluids. However, in the high – intensity domain accomplished through filamentation, the medium's nonlinear response becomes important, resulting in the generation of a detectable THz signal [12]. Furthermore, the third – order nonlinear susceptibility can be influenced by the medium's local density, ionization processes, and the presence of free electrons created by powerful laser pulses.

The efficiency of THz generation in the FWM model is significantly affected by phase control between the fundamental and second harmonic waves. In ideal circumstances, the phases of the interacting fields are aligned, guaranteeing that the THz waves generated at multiple points within the filament sum coherently, maximizing the overall THz output. An important issue in this process is dealing with the dispersive nature of air, which causes the phase velocities of the fundamental and second harmonic waves to diverge, thereby complicating phase matching [17]. Adjustments in the relative phase among the fundamental and second harmonic pulses, in combination with the laser's optimal focusing conditions, help in maintaining coherence and minimize phase mismatch. By carefully managing these variables, THz emitting efficiency can be maximized [3].

The Photocurrent model provides an alternate explanation for THz generation, emphasizing the plasma dynamics that take place during two – color laser filamentation. According to this concept, THz radiation is generated by transient currents triggered in the plasma channel created by the intense laser pulses. The fundamental and second harmonic pulses ionize the air, resulting in a plasma in which free electrons are accelerated by the electrical fields of the two – color laser pulses.

The current density **J**(t) induced by the laser pulses in the plasma can be described:

$$\frac{\partial \tilde{\boldsymbol{J}}}{\partial t} + v_c \tilde{\boldsymbol{J}} = \frac{q_e^2 \rho_e}{m_e} \tilde{\boldsymbol{E}} \qquad (2.9)$$

where $v_c = \frac{2\pi}{\tau}$, τ is the electron collision time, m_e and q_e is the electron mass and charge, ρ_e is the concentration of free electrons, and **E** is the electric field of the laser pulses [16]. The motion of free electrons in the plasma, which is induced by the electric fields of the fundamental and second harmonic waves, generates a time – varying current. This transient current, which emits radiation within the THz frequency range, effectively acts as a powerful source of THz radiation [18]. In this model, the phase relation between the fundamental and second harmonic fields has an immense influence on THz generating efficiency. The relative phase controls the direction and magnitude of transient currents, with constructive interference causing stronger THz emission and destructive interference reducing THz output [8]. This phase – sensitive behavior underscores the need for regulating the relative phase of the two laser pulses for optimal THz production [19]. The plasma density is a central parameter in the photocurrent model. High plasma densities often result in more effective photocurrents, which generate more powerful THz radiation. On the other hand, higher plasma density adds complexity since it affects the refractive index of the medium and modifies the relative phase between the fundamental and second harmonic fields [20].

Both the Four – Wave Mixing and Photocurrent models provide helpful knowledge about the mechanisms of THz generation via two-color laser filamentation. The FWM model considers the nonlinear interaction of fundamental and second harmonic waves. The effectiveness of THz generation is determined by the nonlinear susceptibility $\chi^{(3)}$ and the coherence of the interacting waves. This model emphasizes the importance of phase management in preserving coherence and optimizing THz output. Contrary to this, the photocurrent model is based on plasma dynamics caused by dominant laser pulses. It focuses on the transient currents generated in the plasma, with THz radiation coming from the acceleration of free electrons in the time – varying electric fields of the two – color pulses. The phase relationship between the fundamental and second harmonic fields plays a major role in assessing the efficiency of THz generation in this model, as constructive interference of photocurrents leads to increased THz emission. While the two concepts describe independent mechanisms, they are not antagonistic. In practical experiments, both processes may contribute to THz production, with their respective relevance determined by experimental circumstances such as laser intensity, plasma density, and phase control [3].

2.3 Physical Mechanisms of THz Conical Emission

Laser – plasma interactions, especially with femtosecond two – color laser pulses in air, are a well – known method for producing powerful broadband THz fields. This technique creates a plasma filament that produces THz radiation with a characteristic conical form. Understanding the physical mechanisms underneath this conical emission is critical to optimizing THz generation. THz conical emission is caused by phase matching of the fundamental frequency (ω) and its second harmonic (2ω) in the plasma filament. Nonetheless, the phenomenon is more complex, including a number of different factors such as filament length, plasma density, and plasma nonlinearities. In this chapter, we look into the physical parameters that lead to THz conical emission based on theoretical models and experimental validations reported in the literature.

Focusing femtosecond laser pulses (ω and 2ω) in air causes ionization and formation of a plasma filament. The plasma acts as a medium for the nonlinear interaction of the two – color fields, resulting in broadband THz radiation. The primary mechanism behind this THz generation is the breaking of symmetry in the electric field, which generates a photocurrent in the plasma. This current, in turn, produces THz waves. The nonlinear polarization P(x, y, Ω) that contributes to THz radiation is proportional to the local amplitude of the electric field and the phase difference between the two – color fields.

$$P(x, y, \Omega) \propto A(x, y, \Omega) \sin(\theta(z)) \exp(ik_{THz}z) \tag{2.10}$$

where A(x,y,Ω) is the amplitude of the THz field, $\theta(z)$ is the phase difference between ω and 2ω, and k_{THz} is the wavevector of the THz radiation [21]. In two – color filamentation, the phase mismatch between the fundamental and second harmonic fields generates periodic modulation of THz radiation along the filament's length. This modulation leads to the creation of THz radiation in the off – axis direction, resulting in a conical emission pattern. The conical shape results from constructive interference between THz waves emitted at different point sources along the filament.

The dephasing length l_d that maintains coherent relative phase between two fields is given by:

$$l_d = \frac{\lambda}{2(n_\omega - n_{2\omega})} \tag{2.11}$$

where n_ω and $n_{2\omega}$ are refractive indices at the fundamental and second harmonic frequencies, respectively, and λ is the wavelength of the fundamental field [19]. As soon as the filament length surpasses the dephasing length, the natural phase matching happens off – axis, thus producing the characteristic conical emission. The angle θ_p at which THz radiation peaks can be approximated as:

$$\cos(\theta_p) = 1 - \frac{\lambda}{2l_d} \tag{2.12}$$

The non – uniformity of the plasma along the filament further supports the off – axis phase matching requirement. As the plasma density changes along the filament, the phase of the emitted THz radiation also shifts, contributing to the conical far – field distribution [19].

The experimental confirmation of THz conical emission has been thoroughly investigated. You et al. (2012) demonstrated that THz radiation from two – color laser-induced plasma filaments produces a conical emission pattern, with the emission angle dependent on the filament length and THz wave frequency. Their studies revealed that the THz production increases with filament length, even after the dephasing length [19].

The conical emission can be described as an interference effect. As the laser pulses propagate through the plasma filament, THz waves produced at multiple points along the filament interact constructively in the off-axis direction. The angle of peak THz emission can range from 4° to 7° depending on the THz frequency [19]. Gorodetsky et al. (2014) expanded on this understanding by considering the effects of plasma density variation along and across the filament. Their model considers the phase variations that THz radiation undergoes as it passes through the plasma. This phase change causes destructive interference in the forward direction, which suppresses on – axis THz emission and creates a conical spatial profile [21]. Their study proposed a comprehensive framework to explain the physical principles behind THz conical

emission. Their model includes the concept of plasma opacity, which states that THz radiation at frequencies lower than the plasma frequency cannot pass through the plasma. The equation relates plasma frequency ω_p to plasma electron density N_e [22]:

$$\omega_p = \sqrt{\frac{4\pi e^2 N_e}{m_e}} \tag{2.13}$$

where e is the electron charge and m_e is the electron mass. For typical plasma densities $N_e \sim$ 10^{16} to 10^{18} cm^{-3}, the corresponding plasma frequencies range from 1 to 3 THz. The model additionally takes into account the spatial variation of plasma density along the filament, which has a substantial impact on phase matching conditions. The resulting THz radiation has a conical pattern, with the cone angle determined by the plasma density and filament length. Simulations based on this model match well with experimental data, resembling the observed conical emission patterns [21].

The conical emission of THz radiation from two – color laser filaments is controlled by an intricate interplay of nonlinear optical elements such as phase matching, plasma density modulation, filament length, broadband spectral components, and the focal length of the focusing lens. The commencement of conical emission is determined by phase matching between the fundamental and second harmonic fields, whereas plasma density and filament length have an impact on THz yield and emission angle. The broadband nature of THz radiation causes angular dispersion, which further shapes the conical profile. In the Chapter 3 that follows, we are going to look at other approaches for altering and customizing the THz beam profile. Because the conical emission is caused by interference patterns within the filament, altering the filament geometry allows for more control over the THz beam profile. This paves the way for more advanced THz beam shaping techniques, which will be covered in depth in the chapter that comes next.

2.4 Theoretical Model of THz Interference Pattern

The theoretical model provided here offers a qualitative understanding of the spatial interference patterns produced by these sources, offering insight into the nature of THz beam shaping during filamentation that we will discuss later in Chapter 3. This model perceives the plasma filament as an array of 20 distinct point sources, each generating monochromatic radiation at 4 THz.

The plasma density is assumed to follow a Gaussian distribution, which is an accepted estimate for laser-induced filamentation in air. The density is highest in the center of the filament and drops proportionately towards its edges, according to the following relationship:

$$\rho(z) = \rho_{min} + (\rho_{max} - \rho_{min}) \exp\left(-\frac{z^2}{0.1L_{fil}^2/\sqrt{2}}\right) \tag{2.14}$$

here, $\rho(z)$ denotes the plasma density at point z, with ρ_{min} and ρ_{max} representing the minimum and maximum densities, respectively, and L_{fil} referring to the filament length [23]. The plasma frequency, ω_p, which is determined by the local plasma density, characterizes the natural oscillation frequency of the electrons in the plasma as expressed in Equation 2.13.

The interference patterns that result from the interaction of the emitted THz waves are estimated using the superposition principle, which states that the total electric field at an

observation point is the sum of the electric fields produced by each source. The electric field at an exact spot, denoted by (x, y, z), can be described as:

$$E(x, y, z) = \sum_{i=1}^{N} \frac{A_i}{r_i} \cos\left(i(kr_i + \varphi_i)\right) \tag{2.15}$$

In this formulation, A_i is the amplitude of the field, r_i is the distance between the observation point, k is the wavenumber (with a wavelength of about 75 µm at 4 THz), and φ_i is the phase of the i-th source. The intensity at the observation position is then determined using the square of the magnitude of the total electric field.

The phase of the THz radiation released by the plasma filament changes as it passes through areas with varied plasma density. The refractive index of the plasma is determined by the plasma frequency $\omega_p(z)$ and the frequency of THz radiation ω. The refractive index, n(z), is represented by the equation below:

$$n(z) = \sqrt{1 - \left(\frac{\omega_p(z)}{\omega}\right)^2} \tag{2.16}$$

As the THz radiation travels through the plasma, the refractive index modulates the phase of the waves, leading to variations in the interference pattern. The phase shift $\theta(z)$ at various places along the filament is modified iteratively using the refractive index difference between the fundamental THz frequency and its second harmonic:

$$\theta_j = \theta_{j-1} + \frac{\Delta n_j \omega}{c} \Delta z \tag{2.17}$$

here, Δn_j is the refractive index difference, ω is the angular frequency, $c=3\times10^8$ m/s is the speed of light, and Δz is the step size along the filament. In addition to phase modulation, the model considers amplitude modulation of the THz radiation as a result of cumulative phase shifts throughout the filament. The amplitude modulation is expressed as:

$$Modulation(z) = \sin\left(\theta(z) + \theta_0\right) \tag{2.18}$$

the cumulative phase at location z is denoted by $\theta(z)$, while θ_0 represents the initial phase. This sinusoidal modulation controls the intensity variation as the THz radiation passes along the
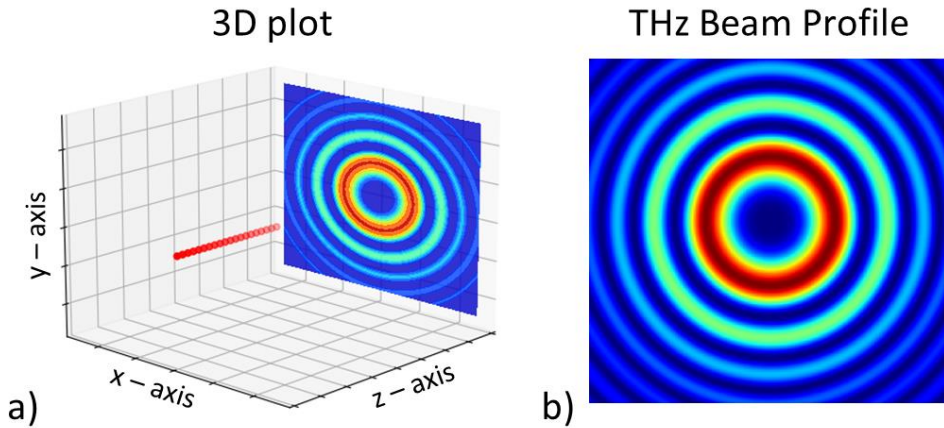

Figure 2.5: a) 3D plot of the filament and emitted THz beam profile (v = 4 THz, filament length = 1.5 mm). b) Corresponding THz beam profile.

filament, introducing constructive and destructive interference that determines the observed intensity distribution. The combination of phase and amplitude modulation explains how the THz beam transforms when it interacts with the plasma [24].

Figure 2.5 shows the theoretical interference pattern for a single THz filament at 4 THz. Part (a) depicts the filament's three – dimensional structure as well as the projected THz radiation pattern. The filament, shown in red, generates THz radiation, resulting in an interference pattern as anticipated by the model. Part (b) of the picture depicts the resulting THz beam profile in the plane perpendicular to the filament, revealing alternating rings of constructive and destructive interference. These rings result from the superposition of the THz waves generated by the point sources.

This theoretical model is intended to provide a qualitative understanding of the interference patterns created by THz radiation from plasma filaments. By representing the plasma as discrete point sources of radiation, the model simplifies the complex dynamics of plasma interactions while keeping the fundamental physics laws underlying THz radiation behavior. The resulting interference patterns provide vital information on the general properties of THz beam shaping. Although the model does not aim for quantitative precision, it is mostly in line with experimental data and serves as a valuable tool for understanding the key characteristics of THz radiation in plasma filaments.

References

1. Träger, F. (2007). *Springer handbook of lasers and optics*. Springer.

2. Weinberger, P. (2008). John Kerr and his effects found in 1877 and 1878. *Philosophical Magazine Letters - PHIL MAG LETT*, *88*, 897–907. https://doi.org/10.1080/09500830802526604

3. *Femtosecond filamentation in transparent media—ScienceDirect*. (n.d.). https://www.sciencedirect.com/science/article/pii/S037015730700021X

4. Kelley, P. L. (1965). Self-Focusing of Optical Beams. *Physical Review Letters*, *15*(26), 1005–1008. https://doi.org/10.1103/PhysRevLett.15.1005

5. Bergé, L., Skupin, S., Nuter, R., Kasparian, J., & Wolf, J.-P. (2007). Ultrashort filaments of light in weakly ionized, optically transparent media. *Reports on Progress in Physics*, *70*(10), 1633. https://doi.org/10.1088/0034-4885/70/10/R03

6. Chin, S. L., Talebpour, A., Yang, J., Petit, S., Kandidov, V., Kosareva, O., & Tamarov, M. P. (2002). Filamentation of femtosecond laser pulses in turbulent air. *Applied Physics B: Lasers and Optics*, *74*, 67–76. https://doi.org/10.1007/s003400100738

7. Gaeta, A. L. (2000). Catastrophic Collapse of Ultrashort Pulses. *Physical Review Letters*, *84*(16), 3582–3585. https://doi.org/10.1103/PhysRevLett.84.3582

8. Koulouklidis, A. D. (2016). *Intense Broadband THz Fields from Laser-Plasma Interactions* [PhD Thesis, University of Crete]. https://doi.org/10.12681/eadd/39960

9. Ammosov, M. V., Delone, N. B., & Krainov, V. P. (1986). Tunnel ionization of complex atoms and of atomic ions in an alternating electromagnetic field. *Soviet Journal of Experimental and Theoretical Physics*, *64*, 1191.

10. Keldysh, L. V. (1965). Ionization in the field of a strong electromagnetic wave. In M. V. Sadovskii, *Selected Papers of Leonid V Keldysh* (pp. 56–63). WORLD SCIENTIFIC. https://doi.org/10.1142/9789811279461_0008

11. Chin, S. L., Liu, W., Hosseini, S. A., Luo, Q., Théberge, F., Aközbek, N., Becker, A., Kandidov, V. P., & Kosareva, O. G. (2005). *Intense femtosecond laser filamentation: Physics and applications*. *26*(3).

12. Boyd, R. W. (2008). *Nonlinear Optics (Third Edition)* (pp. 1–67). Academic Press. https://doi.org/10.1016/B978-0-12-369470-6.00001-0

13. Shen, Y. R. (1984). *The Principles of Nonlinear Optics*. Wiley.

14. *Fundamentals of Terahertz Devices and Applications | Wiley*. (n.d.).

15. Saleh, B. E. A., & Teich, M. C. (2019). *Fundamentals of photonics* (Third edition). Wiley.

16. Agrawal, G. P. (2007). *Nonlinear Fiber Optics*. Academic Press.

17. Butcher, P. N., & Cotter, D. (1990). *The Elements of Nonlinear Optics*. Cambridge University Press. https://doi.org/10.1017/CBO9781139167994

18. Wu, Q., & Zhang, X.-C. (1997). Free-space electro-optics sampling of mid-infrared pulses. *Applied Physics Letters*, *71*(10), 1285–1286. https://doi.org/10.1063/1.119873

19. You, Y. S., Oh, T. I., & Kim, K. Y. (2012). Off-Axis Phase-Matched Terahertz Emission from Two-Color Laser-Induced Plasma Filaments. *Physical Review Letters*, *109*(18), 183902. https://doi.org/10.1103/PhysRevLett.109.183902

20. Zhang, X.-C., & Xu, J. (2010). *Introduction to THz Wave Photonics*. Springer US. https://doi.org/10.1007/978-1-4419-0978-7

21. Gorodetsky, A., Koulouklidis, A. D., Massaouti, M., & Tzortzakis, S. (2014). Physics of the conical broadband terahertz emission from two-color laser-induced plasma filaments. *Physical Review A*, *89*(3), 033838. https://doi.org/10.1103/PhysRevA.89.033838

22. Panov, N. A., Kosareva, O. G., Andreeva, V. A., Savel'ev, A. B., Uryupina, D. S., Volkov, R. V., Makarov, V. A., & Shkurinov, A. P. (2011). Angular distribution of the terahertz radiation intensity from the plasma channel of a femtosecond filament. *JETP Letters*, *93*(11), 638–641. https://doi.org/10.1134/S0021364011110099

23. Wu, H.-C., Meyer-ter-Vehn, J., Ruhl, H., & Sheng, Z.-M. (2011). Terahertz radiation from a laser plasma filament. *Physical Review E*, *83*(3), 036407. https://doi.org/10.1103/PhysRevE.83.036407

24. Zhang, Z., Liu, Z., Wang, S., Lu, C., Fan, Z., Kostin, V. A., & Liu, Y. (2023). Spectral tailoring of the terahertz radiation from air plasma excited by two-color femtosecond pulses. *Applied Physics Letters*, *123*(3), 031108. https://doi.org/10.1063/5.0153490

Chapter 3

Beam Shaping: Experimental Technique

3.1 Spatial Light Modulators (SLMs)

3.1.1 Liquid Crystal Light Modulators

Liquid Crystal Spatial Light Modulators (LC – SLMs) represent pivotal devices in the field of modern optics, offering the ability to dynamically control light beams. These modulators have been employed in a multitude of fields, including, adaptive optics, holography, and optical communication [1]. The fundamental functionality of LC – SLMs hinges on the modulation of light properties, such as amplitude, polarization, and phase, which is enabled by the electro – optic characteristics of liquid crystals [2].

The fundamental structure of an LC – SLM comprises a layer of liquid crystals positioned between a transparent electrode and a backplane, typically constructed using CMOS (Complementary Metal – Oxide – Semiconductor) technology [3]. The CMOS backplane provides the requisite electric field control to vary the refractive index of the liquid crystal layer.
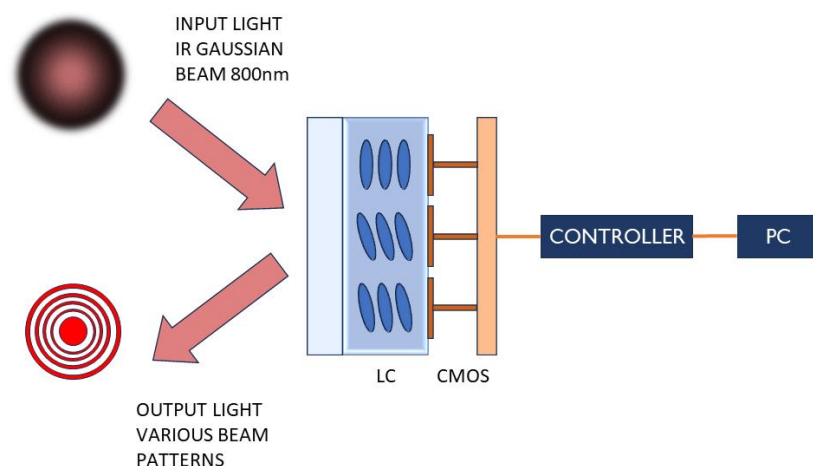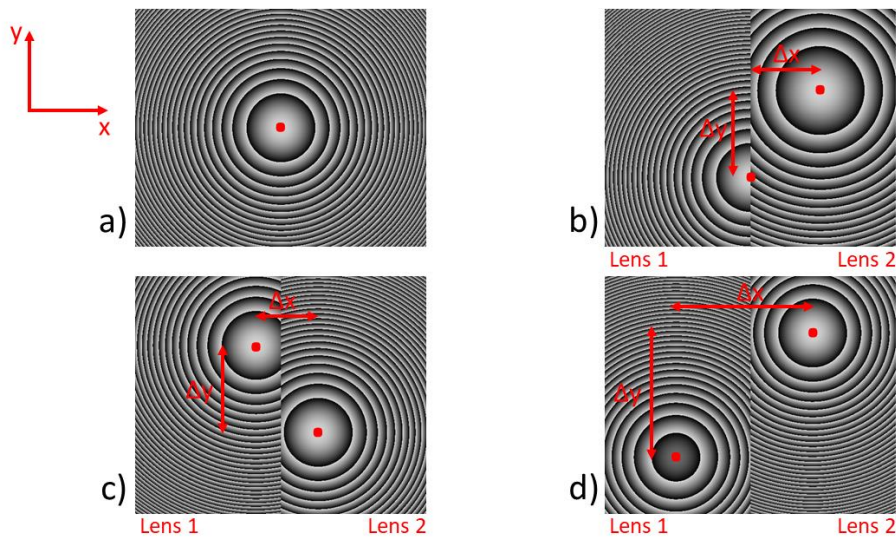

Figure 3.1: A schematic representation of the liquid crystal spatial light modulator [where LC is Liquid Crystal, and CMOS is Complementary Metal – Oxide – Semiconductor].

Figure 3.1 illustrates a schematic representation of an LC – SLM system, wherein an infrared (IR) Gaussian beam is transformed into a plethora of output beam patterns.

The operation of an LC – SLM is based on the distinctive electro – optic properties of liquid crystals, which exhibit characteristics of both liquids and solid crystals. The application of an electric field results in a change in the orientation of the liquid crystal molecules, thereby affecting the material's refractive index. This alteration in refractive index modulates the phase of the incident light. By controlling the electric field across the pixelated backplane, a spatially varying refractive index profile is created, enabling precise phase modulation of the light beam [1]. The Hamamatsu LCOS – X10468 that we used in our experiment is an example of an advanced LC – SLM. It has a high resolution and a fast response time, which makes it suitable for real – time applications. These devices are driven by algorithms that compute the desired phase profile, which is then translated into voltage patterns applied to the liquid crystal layer. This process allows for dynamic and accurate control of the light beam properties [3].

In the present study, an LC – SLM was employed to modulate an IR Gaussian beam derived from a Ti:Sapphire laser system. The laser operated at a central wavelength of 800 nm, with a repetition rate of 1 kHz, a bandwidth of 50 nm, and a pulse energy of up to 2 mJ. The aim was to generate two filaments in the air and manipulate their phase, spatial positioning, and interference. The application of spherical phase masks to the SLM enables the focusing of the input beam to specific points, thereby emulating the functionality of lenses with a focal length of 1200 mm. When the phase mask is divided into two regions with disparate centers, it functions as two distinct lenses, resulting in the generation of two discrete filaments. This configuration facilitates the precise regulation of the relative positions and interactions of the filaments [4].

The phase masks utilized in the experimental procedure were designed with the objective of focusing the incoming infrared (IR) beam. A splitting mask is applied to create an offset between two focal points, whereas a single-phase mask functions as a lens with a fixed focal length. To generate and control multiple filaments, this dual-lens configuration is mandatory. Some of the SLM phase mask designs that we used in our experiment are shown in *Figure 3.2*. The generation of more than one filament process can be manipulated by modifying the focal

Figure 3.2: SLM phase masks with a) Δx=0 μm Δy=0 μm f=1200 mm , b) Δx=2800 μm Δy=3500 μm f1=1200 mm f2=2000 mm , c) Δx=2500 μm Δy=-3500 μm f1,2=1200 mm , d) Δx=5500 μm Δy=5000 μm f1,2=1200 mm φ1=π rads.

lengths f_1, f_2 and mask settings (Δx), (Δy), as demonstrated by the different phase mask patterns (a), (b), (c), (d). These masks' flexibility enables exact control over the filament and beam positions.

Figure 3.2 shows how we may change numerous parameters on the phase masks, including the x and y axis offset, focal length, and initial phase in the center. Typically, the middle of the mask has a phase of zero. Single phase mask (*Figure 3.2a*): with $\Delta x=0$ and $\Delta y=0$, the phase mask, with a focal length f=1200 mm, is focusing the IR beam on a single point, creating a single filament. This configuration is straightforward, where the entire phase mask acts as a single lens. *Figure 3.2b, Figure* 3.2c, and *Figure* 3.2d show offset phase masks. By adding offsets (Δx) and (Δy) to phase masks, we created dual filaments. For instance, in Figure 3b, offsets of $\Delta x=2800$ μm and $\Delta y=3500$ μm with focal lengths $f_1=1200$ mm and $f_2=2000$ mm resulted in two filaments with unique spatial separation. Similarly, in *Figure 3.2c* and *3. Figure* 3.2d, we can see how changing the offsets and focal lengths gives you exact control over the filament placements. The SLM's flexibility and precision were essential in attaining the required filamentation. By carefully designing and applying phase masks, we were able to generate complicated interference patterns and control the spatial dynamics of filaments.

The basic idea for the operation of LC – SLMs is the modulation of the phase of light waves flowing through the liquid crystal layer. When light suffers a change in refractive index, its phase changes according to the relationship:

$$\Delta\varphi = \frac{2\pi d\Delta n}{\lambda} \tag{3.1}$$

where, $\Delta\phi$ is the phase change, Δn is the change in refractive index, d is the thickness of the liquid crystal layer, and λ is the wavelength of the incident light. Changing Δn with an electric field can encode different phase profiles into the light beam.

The spatially variable phase profiles produced by the LC – SLM can be customized to resemble optical elements such as lenses, prisms, and gratings. In our experiment, phase masks were used to concentrate the IR beam in specified positions, resulting in lenses with the necessary focal lengths. When the phase mask is divided into two sections with different centers, it functions as two distinct lenses with adjustable separation, allowing the formation of multiple filaments. The concept of utilizing phase masks to control laser beam propagation is based on Fourier optics principles. The far – field pattern of a beam going through a phase mask is determined by the Fourier transform of the phase mask's transmission function [5]. The application of LC – SLMs in our experiment revealed their ability to control and shape laser beams for THz applications. By accurately adjusting the phase of an IR Gaussian beam, we were able to create and manipulate multiple laser filaments in the air. LC – SLMs are invaluable tools for advanced optical experiments and applications due to their flexibility and precision [1].

3.2 Experimental Setup

The experimental setup depicted in *Figure 3.3* was devised for the purposes of this study. Starting from the top right, the source was a Ti:Sapphire laser system, which is capable of producing a Gaussian beam with a center wavelength at 800 nm, a bandwidth of 50 nm, a pulse energy of up to 2 mJ, a 35 fs pulse duration, and a repetition rate of 1 kHz. The beam splitter (BS) was positioned in such a way that only a percentage of the initial beam would be transmitted to the spatial light modulator (SLM, Hamamatsu). This was due to the damage
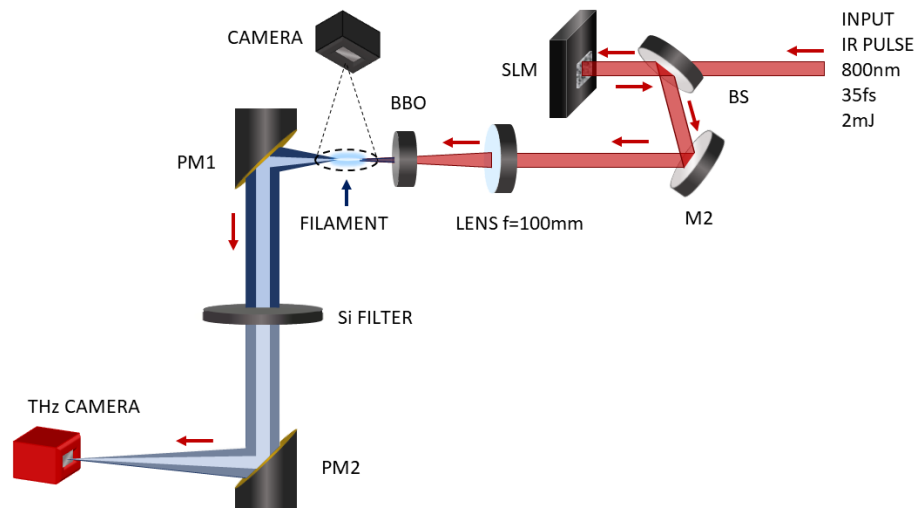
Figure 3.3: A schematic representation of the top view of the experimental setup [where BS; Beam Splitter, M; Mirrors, PM; Parabolic Mirrors and BBO; the β – Barium Borate type crystal, producing the second harmonic].

threshold of the device. So, the incoming pulse is incident on the SLM, which has exerted a spherical phase mask with a focal length of f = 1200 mm, exhibiting a behavior similar to that of a lens. Subsequently, the beam is guided through optical elements to the predetermined path, where it is focused by a lens with a focal length of f = 100 mm. The focal length of the lens was selected to ensure that the intensity of the beam is sufficiently increased to facilitate the generation of a substantial plasma in air at the desired location. A β – Barium Borate (BBO) type crystal with a thickness of 50 μm was positioned between the lens and the plasma in order to facilitate the second harmonic generation (frequency 2ω) of the input pulse (frequency ω). Afterwards, the entire filamentation process occurs, resulting in the generation of THz radiation, as previously discussed in Chapter 2. A pair of off – axis parabolic mirrors was employed to collect, collimate, and re – focus the forward THz radiation from the plasma, thereby enabling real – time monitoring of the THz profile with a THz imager camera (Rigi S2, THz Swiss, Detector: uncooled FPA micro – bolometer array). It should be noted that a silicon (Si) wafer was employed to attenuate the irradiance, thus preventing damage to the optical elements and the camera. Subsequently, the THz camera was positioned 10 mm prior to the focal point of the THz beam. To image the filaments, a charge – coupled device (CCD) camera and imaging optics were utilized.

3.3 Experimental Process and Results

After modulating the infrared (IR) Gaussian beam with the Liquid Crystal Spatial Light Modulator (LC – SLM), we conducted a series of experiments to study the production of THz radiation utilizing two – color laser filamentation in air. As mentioned, the experiment's Ti:Sapphire laser system operated with a central wavelength of 800 nm, a bandwidth of 50 nm, a repetition rate of 1 kHz, and a maximum pulse energy of 2 mJ. The aim of these studies was to understand how different phase masks applied to the SLM affected the generation of laser filaments and the corresponding THz radiation patterns. This research provides insights concerning how to effectively control filamentation and coherent THz emission, which are vital for applications in spectroscopy, imaging, and communication.

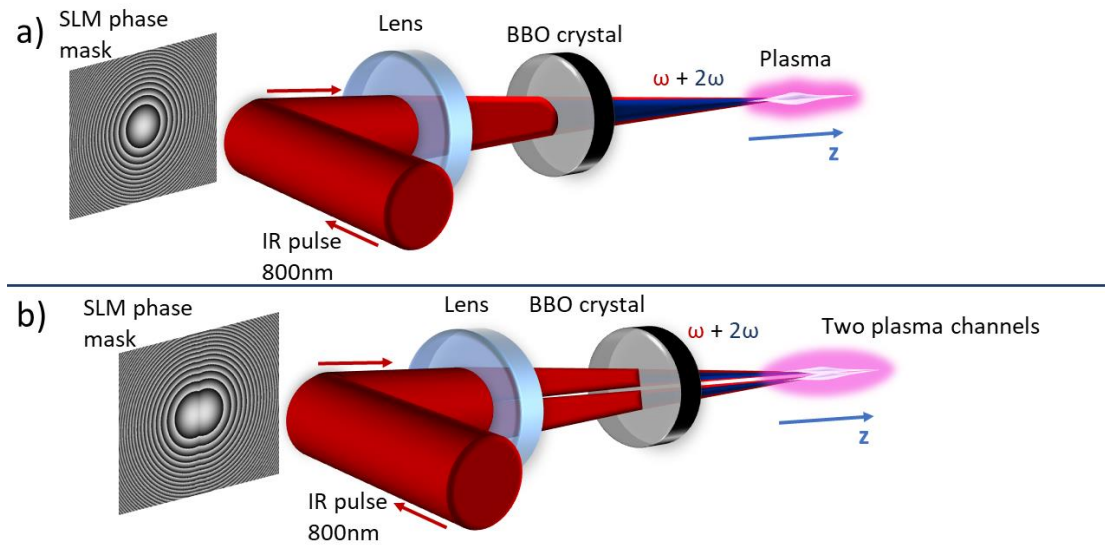### 3.3.1 Single versus Double Filament Generation and THz Emission

Figure 3.4: The generation of the two filaments using different phase masks a) a single filament [Δx=0μm Δy=0μm on SLM], and b) two filaments [Δx=200μm Δy=0μm on SLM] where z is the propagation axis.

In the beginning, a spherical phase mask was centered on the IR beam profile and functioned as a converging lens with a focal length of 1200 mm. This configuration resulted in the development of a single filament in the air. As detailed in Chapter 2, after the filament formed, it produced THz radiation via the two – color laser filamentation process. The THz radiation released in this setup displayed a doughnut – like beam profile, which is characteristic of the conical emission pattern associated with a single laser – induced plasma filament [6]. *Figure 3.4(a)* illustrates the post – SLM setup of the experiment up to the resulting single filament, together with the phase mask that we used.

The radial symmetry in the plasma formed by the filament accounts for the observed doughnut – shaped THz beam profile. The central null in THz radiation intensity is the result of the azimuthal polarization of the emitted THz waves, which is a unique characteristic of THz radiation emitted from a single filament [6].

The experiment's next step was to modify the phase mask by splitting it vertically along its middle and spacing the centers by exactly 200 μm along the x – axis. This adjustment resulted in the development of two separate lenses, each with a focal length of 1200 mm, yielding two closely spaced filaments in the air. *Figure 3.4(b)* represents the design of this experiment, including the phase mask that we used and the corresponding configuration of the two filaments that were formed.

The formation of dual filaments causes complex interactions between the filaments, mostly due to their proximity to one another, which leads to interference effects in the THz field. Each filament is an independent source of conical THz radiation, but the THz waves emitted by these filaments interfere with one another, changing the overall THz radiation pattern. The interference detected in the far field THz beam profile has a two – lobe pattern, which differs from the doughnut shape associated with a single filament. This interference pattern originates from the phase relationship between the THz waves released by the two filaments. When filaments are close together, the overlap of their THz emissions causes both constructive and destructive interference, depending on the relative phase of the waves [7].

The principles of wave interference can be used to comprehend the interference between the THz radiation produced by two closely spaced filaments. Overlapping wavefronts interact when two coherent sources, like laser – induced filaments, are placed close to one another. The phase difference and relative distance between the two sources determine the interference pattern that results [7].

Each filament in a double – filament system can be viewed as a coherent point source of THz radiation. These sources lead to interference in the far field, which modulates the THz intensity and forms patterns like the two – lobe structure we observed in our studies. This pattern arises because, depending on their phase relationship, the THz waves that each filament emits may either enhance or cancel each other out [7]. This characteristic is especially importantfor applications that require precise control over the THz field. By adjusting the distance between the filaments and their relative phases, it is possible to tailor the THz beam profile to specific needs.

The experimental results demonstrate that the phase mask manipulation has a significant impact on filamentation and THz radiation production. When a single filament is created, the THz emission has a symmetric doughnut – shaped beam profile, which corresponds to the plasma's radial symmetry and the emission's conical form. This result aligns with previous models of THz generation from single filaments and emphasizes the significance of symmetry in producing coherent and directed THz radiation [6]. On the other hand, when the phase mask is split in order to create dual filaments, the THz emission profile alters substantially due to interference phenomena. The two – lobe shape seen in far – field THz radiation is the direct result of coherent interference between the THz waves released by each filament. This interference pattern is particularly sensitive to the relative position and phase of the filaments, which permits accurate control of THz radiation characteristics [7].

Figure 3.5 summarizes the aforementioned information by comparing the input phase masks for the single and dual filament cases, as well as the corresponding THz beam profiles. This comparison highlights the versatility of phase mask modification in manipulating filamentation dynamics and adapting THz radiation features to specific applications.
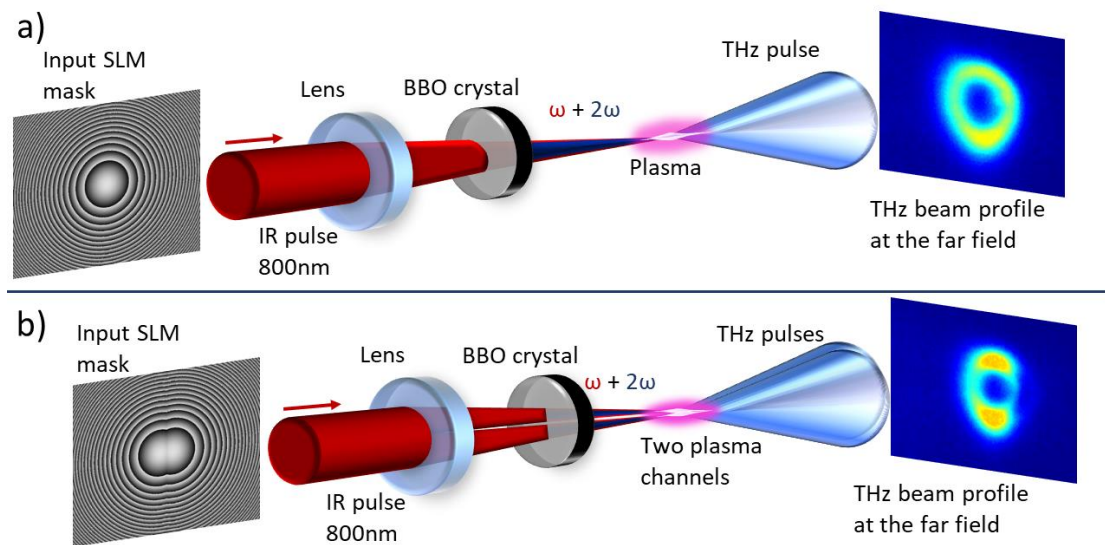
Figure 3.5: THz conical emission from a) a single filament [Δx=0μm Δy=0μm on SLM], classical concept and b) two filaments [Δx=800μm Δy=0μm on SLM].

3.3.2 Steering the THz Beam Profile

This aspect of our study is dedicated to examining the manipulation and control of the two – lobe THz beam profile that arises from the interaction of two laser filaments. As previously stated, these filaments were created by splitting the spherical phase mask used on the LC – SLM and separating the centers by 200 μm along the x – axis. This configuration enabled the formation of two close – spaced filaments in the air, leading to the characteristic two – lobe THz beam profile. We now look into how this beam profile can be steered, offering a way to control the spatial orientation of the THz emission, by varying the relative position of one filament along the y – axis. The split – phase mask generates two laser filaments, each of which interacts nonlinearly, resulting in the two – lobe THz beam profile. By adjusting just one filament on the y – axis, we are able to manipulate the direction of this beam profile. This
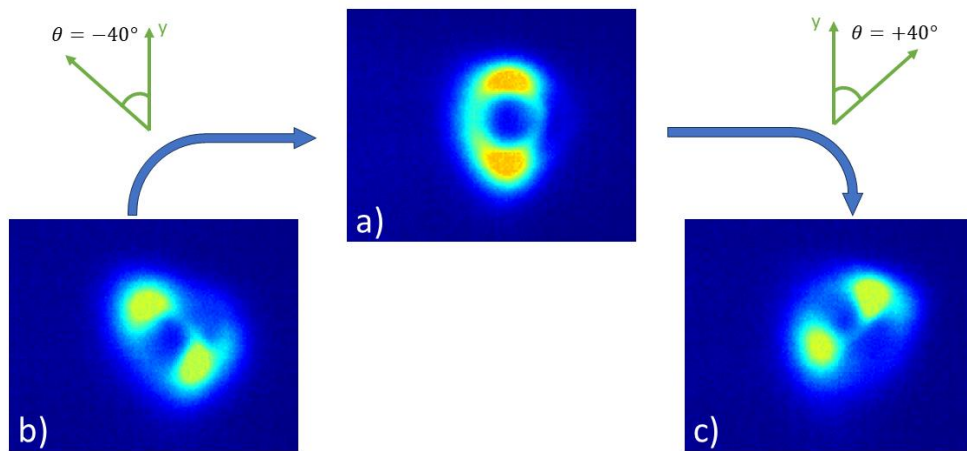

Figure 3.6: The rotation of the beam profile can be achieved by adjusting the two filaments' respective positions a) Δx=200 μm Δy=0 μm, b) Δx=200 μm Δy=-500 μm, c) Δx=200 μm Δy=+500 μm.

movement can be accomplished by adjusting the y – offset of one side of the SLM phase mask, which alters the corresponding position of the filaments and hence the relative orientation of the THz beam.

   Figure 3.6 shows the method of beam steering. The central image (*Figure 3.6a*) depicts an initial two – lobe THz beam profile generated when filaments are aligned symmetrically at a zero y – offset (Δy=0 μm on the SLM's phase mask). This profile is positioned vertically to represent the symmetrical placement of the two filaments along the x – axis. When we introduce a y – offset of Δy=−500 μm to just one of the two filaments (*Figure 3.6b*), the beam profile rotates counterclockwise by an angle of -40°, demonstrating that the constructive and destructive interference areas between the filaments have shifted. Conversely, applying a positive y – offset of Δy=+500 μm (*Figure 3.6c*) leads to the beam profile rotating clockwise by +40°, indicating the beam's sensitivity to filament position.

   The ability to steer the THz beam profile by adjusting the relative position of the filaments exemplifies the level of control that phase mask modulation may provide over THz radiation. The y – offset introduces phase differences that cause the beam profile to rotate, altering the interference pattern between the two filaments.

We recorded THz profiles at various y – offsets ($\Delta y=-500$ μm to $\Delta y=+500$ μm) to observe the continuous evolution of the beam profile. The profiles are shown in *Figure 3.7*. The top row (*Figure 3.7a*) depicts the evolution of the THz beam profile when the x – offset is held constant at $\Delta x=0$ μm and the y – offset is adjusted in steps of 100 μm. This image collection demonstrates the way the THz beam profile shifts from a -40° angle at $\Delta y=-500$ μm to a vertically aligned configuration at $\Delta y=0$ μm, and finally to a +40° angle at $\Delta y=+500$ μm. The gradual rotation observed here reveals a smooth transition in the interference pattern when the filaments' relative y – positions are altered.
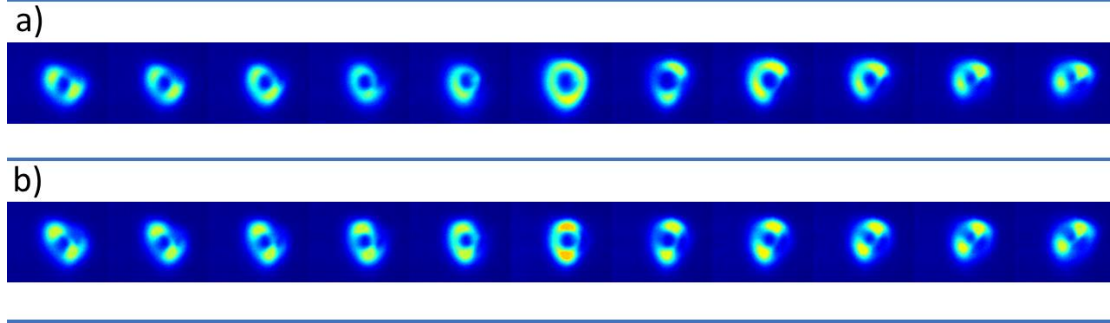
Figure 3.7: The evolution of the shift of the THz profile as the relative vertical distance of the two filaments is altered a) Δx=0 μm and Δy from -500 μm to 500 μm with step 100 μm, b) a) Δx=200 μm and Δy from -500 μm to 500 μm with step 100 μm.

In the bottom row (*Figure 3.7b*), we present the transformation of the THz beam profile when the x-offset is fixed at $\Delta x=200$ μm, with the same y-offset variation. The initial two-lobe configuration at $\Delta y=-500$ μm rotates continuously through multiple orientations as the y-offset is increased. This demonstrates the noteworthy dependency of the THz profile on the precise relative placement of the filaments. The final image in the sequence, at $\Delta y=+500$ μm, shows the beam rotated in a way analogous to the top row, but with only minor modifications due to the initial x – offset. The THz emission pattern's sensitivity to the filaments' relative positions is demonstrated by the beam profile's gradual shift, as seen in *Figure 3.7*. The interference between the THz fields produced by the two filaments varies as the y – offset is adjusted, which causes the beam profile to continuously rotate and reshape.

The manipulation of the THz beam profile by modifying the y – offset is intrinsically linked to the interference and nonlinear interactions between the two filaments. When two filaments are placed close together, their resultant THz fields overlap and interact with one another, leading to a complex interference pattern that forms the apparent beam profile. The direction and shape of this beam profile are significantly dependent on the relative phase and amplitude of the THz fields, which are regulated by the filament positions [7]. As one filament moves along the y – axis, the phase difference between the THz fields changes, causing the interference pattern to change orientation. This rotation demonstrates the phase-sensitive nature of the interference process. The y – offset's phase shifts affect the constructive and destructive interference areas, thereby determining the direction of THz emission. The continuous evolution of the THz beam profile as the y-offset is varied, as illustrated in *Figure 3.7*, points out the adaptability of this steering mechanism. The ability to achieve an extensive range of beam profiles by merely adjusting the position of each of the filaments indicates the potential of phase mask modulation to improve the performance and versatility of THz sources.

3.3.3 A Review of the Correlation Between Theoretical Predictions and Experimental Results

In this section of the study, it is vital to compare the experimental and theoretical results. The theoretical ones are generated by the model detailed in Chapter 2. The theoretical model given in previous sections serves as a framework for predicting the spatial and spectral features of THz radiation produced by laser filament interactions. We will compare theoretical predictions to experimental outcomes, with a focus on the agreement observed in the two situations offered, emphasizing the importance of linear interference in accurately predicting experimental results.

It is crucial to take into account that the theoretical interference model described in this work is mainly a qualitative tool for understanding the mechanisms that shape the THz beam profile. While the model successfully represents the fundamental principles of linear interference and makes predictions that closely match experimental data, it is designed to provide a general understanding of THz radiation's spatial characteristics rather than a rigorous quantitative analysis. The model simplifies certain aspects of the complicated interactions involved, including plasma dynamics, which are addressed in a generalized manner. Thus, while the model is highly beneficial for interpreting experimental results and guiding future studies, it should be considered a qualitative framework that emphasizes the major elements influencing THz beam profile formation.
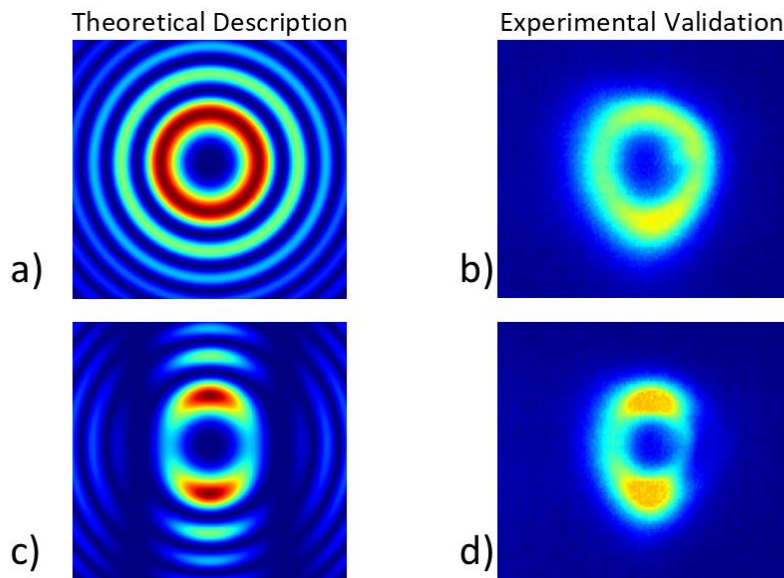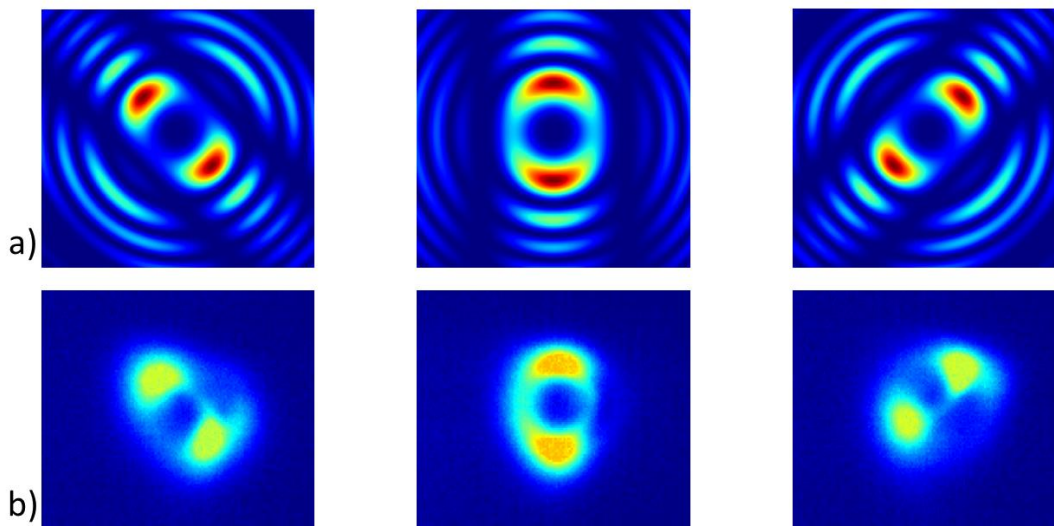

Figure 3.8: Comparison: THz beam profile from single filament (top) and two filaments (bottom) a) theoretical description (frequency ν=4THz, length of the filament l=1.5 mm), b) experimental data, c) theoretical description (ν=4THz, length of filaments l=1.5 mm with a separation Δx=60 μm), d) experimental data.

Figure 3.8 shows a comparison of theoretical predictions and actual data for THz beam profiles produced by a single filament (top row) and two filaments (bottom row). The theoretical description (left column) was constructed using the already – explained interference model, while the experimental validation (right column) was achieved via measurements. The theoretical model predicts a concentric ring pattern for the THz beam profile produced by a single filament, as shown in *Figure 3.8a*. This pattern results from the filament's radial symmetry, which creates a doughnut – shaped beam profile resulting from the constructive and destructive interference of THz waves radiating outward from the filament. *Figure 3.8b* depicts experimental data that closely approximates the theoretical prediction, with a doughnut – shaped profile recorded. The slight variations between the predicted and achievable profiles can

be attributable to experimental noise and slight imperfections in the filament's alignment. However, the general agreement between the two suggests that the model is accurate in predicting the beam profile for a single filament.

When two filaments are separated by 60 μm along the x – axis, the theoretical model predicts a two – lobe THz beam profile, as seen in *Figure 3.8c*. This pattern is the consequence of linear interference between the THz waves emitted by each filament. The constructive interference occurs along the axis that connects the two filaments, whereas the destructive interference occurs perpendicular to this axis, resulting in this particular two – lobe shape. The experimental data, shown in *Figure 3.8d*, is in great accordance with the theoretical prediction. The experimentally recorded two-lobe pattern demonstrates the model's ability to precisely anticipate the consequences of linear interference between two filaments. Minor discrepancies in the intensity distribution across the lobes can be attributed to subtle variations in filament intensities.

This comparison highlights how the observed data closely correspond to the theoretical predictions given by this interference model. The agreement between experiment and theory suggests that the model accurately describes how linear interference influences the THz beam profile.

Figure 3.9: Comparison: THz beam profile rotation from two filaments a) theoretical description (v=4THz length of the filament l=1.5 mm, Δx=60 μm Δy= ± 60 μm) b) experimental data.

Figure 3.9 compares theoretical predictions to experimental observations for the rotation of a THz beam profile created by two filaments. This comparison focuses on how the beam profile changes as one filament's relative vertical location (y – offset) varies. The theoretical model indicates that changing the y – offset from -60 μm to +60 μm causes the two – lobe THz beam profile to rotate. At the middle position (0 μm offset), the lobes are vertically aligned, but when the offset increases or decreases, the lobes rotate due to the changing phase interaction between the two filaments' THz waves. *Figure 3.9a* depicts a sequence of theoretical images showing the expected rotation of the THz beam profile. The theory indicates that the beam profile rotates counterclockwise when the y – offset is negative and clockwise when the y – offset is positive, which aligns with the linear interference pattern dictated by the filaments' associated phases. The experimental data in *Figure 3.9b* reveal an analogous rotation of the THz beam profile as the y – offset of the filaments is changed. The main image (middle of the bottom row) displays

aligned filaments (0 μm y – offset) with a vertical two – lobe pattern. As the y – offset changes, the lobes rotate with respect to theoretical predictions. The remarkable agreement between experimental and theoretical results reveals that the THz beam profile rotates predominantly because of the linear interference that exists between the two filaments. The experimental results validate the model's prediction that minor changes in the relative position of the filaments may lead to major alterations in the THz beam profile.

This comparison not only proves that the experimental data confirm the theoretical model, but it additionally demonstrates how linear interference plays an essential role in influencing the spatial properties of THz radiation. The observed ability to steer the THz beam by modifying the filament positions shows the model's usefulness for applications that call for accurate control over the THz field.

In overall terms, the comparisons between theoretical predictions and practical results in *Figure 3.8* and *Figure* 3.9 suggest that the interference model is an efficient tool for understanding the behavior of THz radiation emitted by laser filaments. The level of agreement in each case shows the model's qualitative precision in describing the role of linear interference as a fundamental mechanism controlling the spatial distribution of THz radiation. The model is aimed at offering an in – depth comprehension of how the experimental results correlate with the appropriate theoretical predictions, assuming linear interference. However, in cases where the two filaments interact nonlinearly – for example, when they are in close proximity and create a superfilament – this model cannot effectively anticipate the subsequent THz radiation.

3.3.4 Comparison of THz Beam Profiles from Single and Double Filamentation: Nonlinear Interference and Energy Enhancement

In the continuous research of THz radiation generated through laser filamentation, one of the primary areas of attention is the contrast between the THz beam profiles produced by a single filament versus the ones produced by a closely spaced two – filament system. The following section will go over the experimental data that show the changes in energy distribution and beam profiles between these two configurations, with a focus on the consequences of nonlinear interference and superfilamentation. The IR Gaussian beam was controlled using an LC – SLM loaded with a vertically split phase mask. This mask was created to separate the centers of the spherical phase sections by 200 μm across the x – axis, like we did earlier. Each side of the phase mask functioned as a separate lens with a focal length of 1200 mm, resulting in two closely spaced filaments in the air. This configuration was designed to look into the interference between the two filaments and its impact on the generated THz radiation, mainly in the sense of energy distribution and beam profile shape.

Figure 3.10 shows a direct comparison of THz beam profiles and filament configurations for both a single filament and a two – filament system. The upper left image in *Figure 3.10a* displays the THz beam profile generated by a single filament, which has the classical doughnut – like shape, confirming conical THz emission. The bottom left image shows the comparable filament form, which is a single, symmetrical filament. The energy of the THz radiation produced in this case, E_{THz1}, has been estimated to be 8.36 μJ. The top right image in *Figure 3.10b* depicts the two – filament system's THz beam profile. Unlike the single filament example, the THz beam profile has a two – lobe shape, reflecting a far more complicated interference pattern. The corresponding filament system, seen in the bottom right figure, shows two close – connected filaments with notable overlap, suggesting the development of a superfilament. The THz radiation energy in this two – filament system, E_{THz2}, was measured to be 9.80 μJ. The

observed energy increase ($E_{THz2} > E_{THz1}$) suggests that the two – filament system does not just produce additive THz radiation but rather a nonlinear interaction between the filaments. This interaction results in the formation of a superfilament, in which the energy of the THz radiation is greater than the sum of the individual contributions from the two separate filaments.
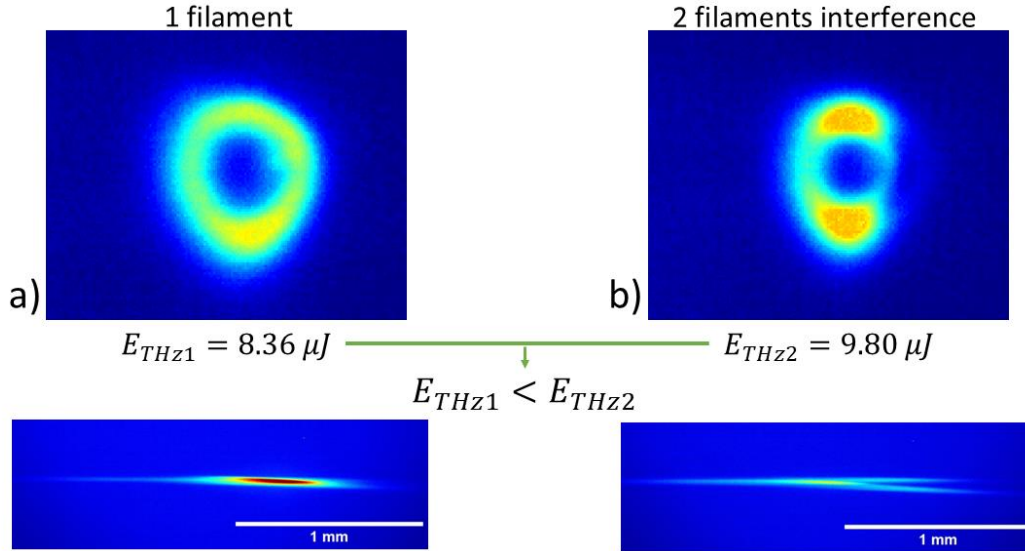

Figure 3.10: *Comparison of THz beam profiles, measured energy, and corresponding filaments for: a) a homogeneous energy distribution from a single filament (Δx=0 μm, Δy=0 μm), and b) the energy distribution resulting from interference between two filaments (Δx=0 μm, Δy=200 μm).*

Figure 3.10 demonstrates that the two-filament system provides a significantly different THz beam profile and an increased energy output than the single – filament system because of nonlinear interference. This difference is mostly caused by the creation of a superfilament, which develops when the two closely spaced filaments interact sufficiently strongly to merge into a single, more powerful plasma channel. This nonlinear interaction is directly responsible for the two – lobed THz beam profile seen in the two – filament system. The increased energy production and altered beam shape indicate that the superfilament serves as a far more effective source of THz radiation, with interference between the filaments contributing to energy redistribution within the beam.

3.3.5 Nonlinear Interference between the Two Filaments

This section of our study looks into the complex interactions among multiple laser filaments and the resultant nonlinear effects, with a specific emphasis on the formation of a superfilament, in the context of THz radiation generation through laser filamentation in air. We will focus on the case where we receive the characteristic two – lobe – shaped profile of the THz beam that we discussed above. Using the LC – SLM, we split the IR Gaussian beam into two spatially separated filaments using a phase mask that operated as two lenses, each with a focal length of 1200 mm. The phase mask was split vertically, with the centers of the spherical phase masks spaced by 200 μm across the x – axis of the SLM. This approach allowed us to gain insight into both the independent THz emissions from each filament and the nonlinear interactions that take place when the filaments coexist, which leads to the formation of a superfilament.

In order to examine the THz radiation emitted by each filament separately, we adjusted the LC – SLM to deactivate one side of the phase mask at a time. This method allowed us to isolate the contribution of every single filament, enabling us to measure and record the THz beam

$$E_{THz}^1 = 2.20 \; \mu J \qquad E_{THz}^2 = 3.80 \; \mu J$$
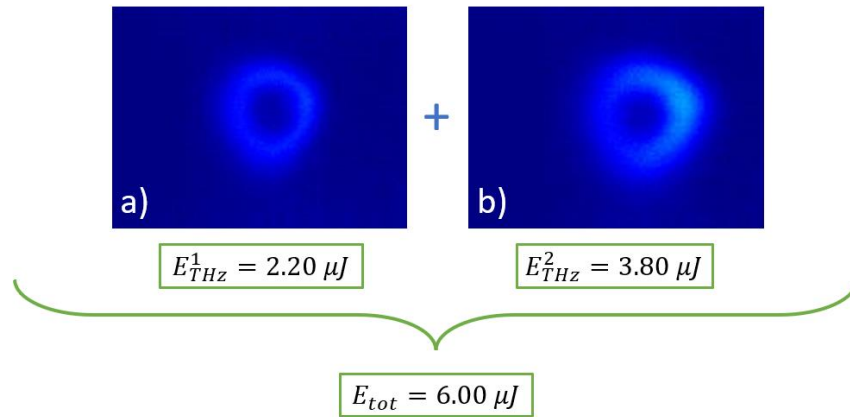
$$E_{tot} = 6.00 \; \mu J$$

Figure 3.11: a), b) THz beam profile and the recorded energy from each separated filament. c) The mathematical addition of the two images and the total energy.

profiles produced by each filament individually, as shown in *Figure 3.11a and Figure* 3.11*b*. The THz radiation from each filament displayed a conical emission pattern, which was analogous with the behavior seen in single – filament THz generation via two – color laser filamentation in air [7].

A key outcome of this experiment is the sharp contrast between the interference pattern that really occurs when both filaments coexist and the THz profile that is added mathematically. The THz beam profile that arises from the simultaneous existence of the two filaments, leading to the distinctive two-lobe interference pattern, was recorded with an energy of 9.80 μJ. In comparison, the THz energies of the two separated filaments, when added, amounted to 6.00 μJ. This difference suggests a nonlinear interaction between the filaments, as the total THz field exceeds the sum of all of its individual components. The nonlinear interaction between the two filaments causes a superposition of the THz fields, which is the direct cause of this pattern and cannot be fully explained by linear addition [7].

In our experiment, the superfilament forms when the two primary filaments overlap. The high electric fields in this region cause significant nonlinear effects. The superfilament possesses various characteristics that are distinct from the individual filaments, such as elevated intensity, altered phase relationships, and amplified THz emission. The intensity of the electric field within the superfilament is significantly higher compared to that of each filament individually. This field augmentation is caused by constructive interference and nonlinear amplification within the overlapping region of the two filaments. The increased field strength in the superfilament region accelerates nonlinear processes, contributing to the observed increase in THz emission.

3.3.6 Redistribution of Energy in the THz Beam Profile

In the ongoing investigation of THz beam shaping through laser filamentation, there is a strong emphasis on the potential to control and redistribute energy effectively within the THz beam profile. The LC – SLM phase mask was used in a similar manner to prior configurations, with each half of the mask functioning as a separate lens with a focal length of 1200 mm. However, in this experiment, the attention was on adjusting the y – axis position of a single side of the SLM's phase mask while maintaining the x – axis alignment. The objective was to see how microshifting the center of the phase mask along the y – axis would influence the energy distribution in the THz beam. In order to accomplish this, the following configurations were

looked at: phase masks are first centered. A single filament was created, resulting in a perfectly even, doughnut – shaped THz beam profile when the centers of the phase masks were precisely aligned (Δx = 0 μm, Δy = 0 μm). Furthermore, adjusting the phase masks. The left side of the THz beam profile was directed by moving the center of one half of the SLM's phase mask by +60 μm along the y – axis. On the other hand, the energy was reallocated to the right side by moving the center along the y – axis by -60 μm. In these configurations, two filaments were produced, and the interaction between them led to the formation of a superfilament.

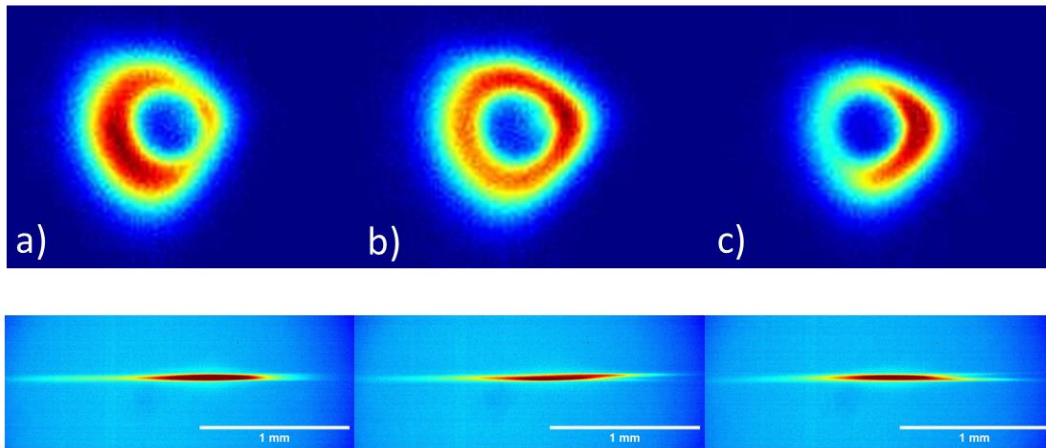*Figure 3.12: Controlling the distribution of energy a) to the left (Δx=0 μm Δy=+60 μm), b) homogeneous (Δx=0 μm Δy=0 μm) c) to the right (Δx=0 μm Δy=-60 μm).*

Figure 3.12 shows a comprehensive representation of the experimental data. The top row *(a, b, and c)* displays the THz beam profiles for the three LC – SLM phase mask configurations. The bottom row shows the longitudinal cross – sections of the laser filaments that produced the THz beam profiles. The *Figure 3.12a* below displays the THz beam profile after shifting the center of the phase mask by +60 μm alongside the y – axis. The thereby produced THz beam profile shows a substantial redistribution of energy to the left. The corresponding filament system (bottom row) portrays two tightly separated filaments with a clear superfilament formation in between. The superfilament is the outcome of a nonlinear interaction between the two filaments, which enhances THz emission in the leftward direction. *Figure 3.12b* shows that aligning the phase mask centers (Δx = 0 μm, Δy = 0 μm) creates a single filament and a homogeneous, doughnut-shaped THz beam profile, as we have already seen. The bottom row represents the corresponding single filament, demonstrating that there is no major nonlinear interaction since only one filament is present. This configuration acts as a reference point for assessing the effects of filament separation and superfilament generation on the THz beam profile. In a similar way, *Figure 3.12c* shows the THz beam profile when the center of the half – phase mask is relocated -60 μm along the y – axis. Here, the energy is redirected to the right side of the THz beam profile. The associated filament structure again demonstrates the presence of two filaments interconnected by a superfilament. The superfilament's effect sends THz energy to the right, showing the ability to manipulate energy distribution within the THz beam using nonlinear interactions.

The results shown in *Figure 3.12* suggest that nonlinear interference effects serve an important role in the observed redistribution of energy within the THz beam profile, especially when the two filaments are brought near together. The idea of the importance of superfilamentation is vital for comprehending the nonlinear energy redistribution seen in these

studies. The superfilament facilitates energy transfer between the two interacting filaments. Depending on the relative phases and intensities of the filaments, this exchange may result in either increased or decreased THz radiation. In the examples shown in (a) and (c) of *Figure 3.12*, superfilament creation causes a directional redistribution of THz energy, which aligns with the way that the center of the half – phase mask is displaced on the y – axis with respect to the other. The above pattern suggests that the observed energy steering is due to nonlinear coupling between the filaments.

3.3.7 THz Beam Profile Manipulation: On – Axis Energy Distribution

One of the primary outcomes of exploring THz beam shaping is the ability to control the spatial distribution of THz radiation in order to attain desired beam profiles. This section focuses on an exceptional circumstance in which THz radiation is almost concentrated on the propagation axis (z – axis), which is a significant achievement considering the typically conical nature of THz emission. The conical emission characteristic of THz radiation, inherent in the two-color laser filamentation process, always leads to off-axis radiation; therefore, the on – axis energy concentration seen in this experiment is exceptionally noteworthy. In order to accomplish this, the SLM phase mask was again vertically split, allowing each half to function as a separate lens with a focal length of 1200 mm. In this configuration, the centers of the spherical phase masks were relocated by -500 μm on the x – axis and 400 μm on the y – axis on the SLM. This deliberate adjustment had been intended to figure out how such an arrangement might affect the final THz beam profile.
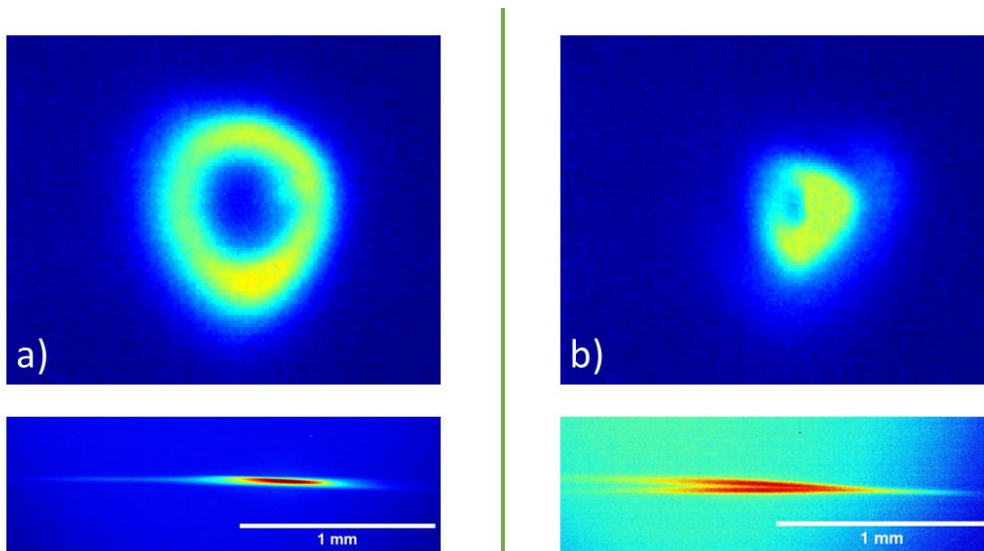
Figure 3.13: The homogeneous distribution of energy (Δx=0 μm Δy=0 μm) and b) almost on – axis energy distribution (Δx=-500 μm Δy=400 μm) and the corresponding filaments.

Figure 3.13 shows the outcome of this experimental configuration. The top row of the picture depicts the THz beam profiles for two different phase mask setups, while the bottom row depicts the laser filaments that generate these THz profiles. *Figure 3.13a* displays the THz beam profile with the phase mask centers aligned (Δx = 0 μm, Δy = 0 μm). As expected, the resulting THz beam profile has a homogenous doughnut – shaped distribution, which is typical of conical THz emission. The corresponding filament system (bottom row) has a single filament, which is in accordance with the symmetrical energy distribution shown in the THz beam profile. *Figure 3.13b* is especially noteworthy since it shows a THz beam profile with energy concentrated almost on the propagation axis (z – axis). Because of the conical nature of THz emission, achieving on – axis radiation is extremely uncommon, making this result

remarkable. The centers of the split – phase mask were moved by -500 μm on the x – axis and 400 μm on the y – axis, resulting in this totally different beam profile. The corresponding filament system (bottom row) shows two separated filaments, which are at different heights. By separating the spherical mask centers by 400 μm along the y – axis on the SLM, the filaments are also separated, limiting close interaction. Because the filament image is a top view, the xz plane is the only perspective from which to observe the filaments. However, this beam profile is the result of the interaction between the THz radiation in the far field, which is released separately by each filament.

The near – on – axis concentration of THz radiation becomes particularly worth mentioning since it differs from the ordinary conical emission pattern reported in most THz – generating configurations. This shows that the phase mask's unique design and the corresponding filament interactions can affect the phase matching conditions, causing the THz radiation to be directed along the propagation axis (z – axis). This finding opens up novel possibilities to control the directionality of THz radiation, which is critical for applications that call for high accuracy.

3.3.8 Unexpected "THz Emojis": The Fun Side of Experimental Physics

During the course of our exploration of THz beam shaping using laser filamentation, we made an unexpected yet humorous discovery. Several images resembling faces or emojis, common in modern digital communication, occurred while analyzing the THz beam characteristics. These profiles, while physically relevant and representing the nature of laser filament interactions, presented an entertaining equivalent to known emoji emotions, adding an element of surprise and fun to an otherwise very technical scientific process.

The top of *Figure 3.14* shows a THz beam profile that is strikingly similar to the iconic devil emoji. In the middle part of *Figure 3.14*, the beam profile reveals an obvious resemblance to the "smiling sunglasses emoji", while at the bottom part of the figure, it bears a similarity to an alien emoji, adding a dimension of humor to our visual analysis. From a scientific standpoint, these THz beam profiles' anthropomorphic features are simply a result of specific filament position configurations and the interplay between their produced THz radiation fields.

In a nutshell, while the phenomenon is rooted in the physics of filament interactions, its likeness to popular emojis connects the abstract world of physics to the pop – cultural symbols of modern communication. It gives a reminder that even when seeking complex scientific knowledge, unexpected joy can be found, making the learning process even more fulfilling.
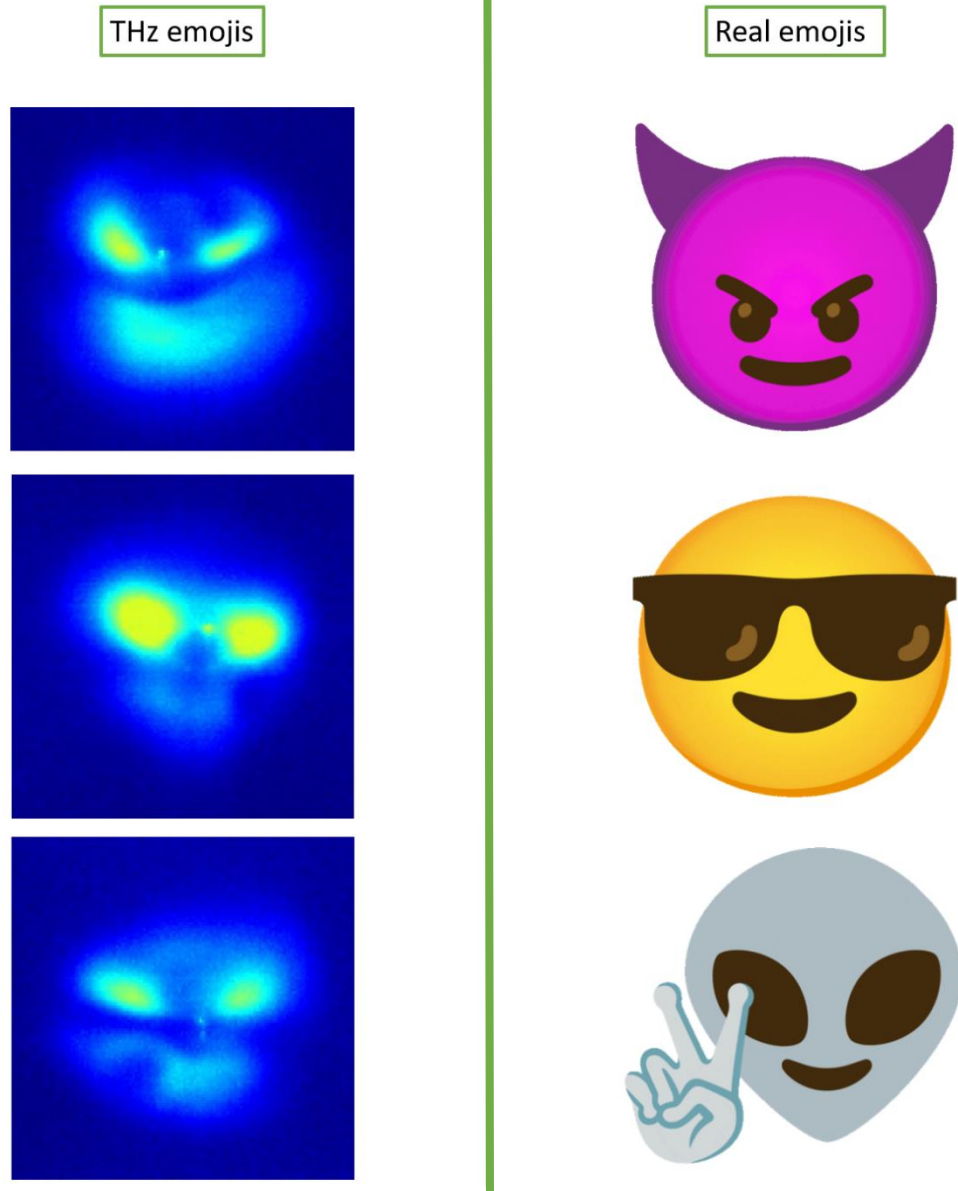
Figure 3.14: THz Emojis versus pop – cult emojis

3.4 Conclusion

This thesis presents a unique and efficient method for shaping terahertz (THz) beams in air through laser filamentation. A spatial light modulator (SLM) was used to modify the phase and spatial distribution of ultrashort laser pulses, allowing the characteristics of the generated THz radiation to be controlled dynamically. This approach has considerable advantages over traditional technologies like diffractive optical elements and metasurfaces, which frequently result in increased system complexity and energy losses. The all-optical technique presented here allows for greater flexibility and precision in shaping the THz beam, making it ideal for a wide range of THz technology applications.

The main results of this study emphasize the ability to create various THz beam profiles by adjusting the configuration of laser filaments. The outcomes revealed that linear and nonlinear interactions between filaments play a key part in shaping the spatial characteristics of the THz beam. For example, the formation of two closely spaced filaments led to different interference patterns, such as the observed two-lobe profile, which can be explained by both constructive and destructive interference effects. Furthermore, the experiments demonstrated the possibility for nonlinear energy enhancement, especially when the filaments were placed close together, resulting in superfilamentation and higher THz output. The ability to manipulate the THz beam profile through electronic phase mask control opens up new applications in THz imaging, communication, and spectroscopy. The experimental results were consistent with theoretical expectations, demonstrating the validity of the model utilized to characterize linear interference and energy redistribution processes.

In conclusion, the study reported in this thesis shows that laser filamentation, when paired with precise manipulation of phase masks, is an effective and versatile tool for shaping THz beams. The results pave the way for future advances in THz technology, particularly in areas requiring fine control over beam profiles. With further improvement, this approach has the potential to deliver considerable advances in scientific research and industrial applications.

References

1. Ivanova, N. L., Onokhov, A. P., Chaika, A. N., Resnichenko, V. V., Yeskov, D. N., Gromadin, A. L., Feoktistov, N. A., & Beresnev, L. A. (1996). Liquid crystal spatial light modulators for adaptive optics and image processing. *Advances in Optical Information Processing VII*, *2754*, 180–185. https://doi.org/10.1117/12.243141

2. Arrizón, V., Méndez, G., & Sánchez-de-La-Llave, D. (2005). Accurate encoding of arbitrary comp[]lex fields with amplitude-only liquid crystal spatial light modulators. *Optics Express*, *13*(20), 7913–7927. https://doi.org/10.1364/OPEX.13.007913

3. Gelbaor Kirzhner, M., Klebanov, M., Lyubin, V., Collings, N., & Abdulhalim, I. (2014). Liquid crystal high-resolution optically addressed spatial light modulator using a nanodimensional chalcogenide photosensor. *Optics Letters*, *39*, 2048–2051. https://doi.org/10.1364/OL.39.002048

4. Béjot, P., Kasparian, J., Henin, S., Loriot, V., Vieillard, T., Hertz, E., Faucher, O., Lavorel, B., & Wolf, J.-P. (2010). Higher-Order Kerr Terms Allow Ionization-Free Filamentation in Gases. *Physical Review Letters*, *104*(10), 103903. https://doi.org/10.1103/PhysRevLett.104.103903

5. Goodman. (n.d.). *Goodman Fourier Optics*. http://archive.org/details/GoodmanFourierOptics

6. Koulouklidis, A. D., Gollner, C., Shumakova, V., Fedorov, V. Y., Pugžlys, A., Baltuška, A., & Tzortzakis, S. (2020). Observation of extremely efficient terahertz generation from mid-infrared two-color laser filaments. *Nature Communications*, *11*(1), 292. https://doi.org/10.1038/s41467-019-14206-x

7. You, Y. S., Oh, T. I., & Kim, K. Y. (2012). Off-Axis Phase-Matched Terahertz Emission from Two-Color Laser-Induced Plasma Filaments. *Physical Review Letters*, *109*(18), 183902. https://doi.org/10.1103/PhysRevLett.109.183902

8. Oh, T. I., You, Y. S., Jhajj, N., Rosenthal, E. W., Milchberg, H. M., & Kim, K. Y. (2013). Intense terahertz generation in two-color laser filamentation: Energy scaling with terawatt laser systems. *New Journal of Physics*, *15*(7), 075002. https://doi.org/10.1088/1367-2630/15/7/075002